JGP Journal of General Physiology

ARTICLE

The M1 and pre-M1 segments contribute differently to ion selectivity in ASICs and ENaCs

Zeshan P. Sheikh[1], Matthias Wulf[1], Søren Friis[2], Mike Althaus[3], Timothy Lynagh[1], and Stephan A. Pless[1]

The ability to discriminate between different ionic species, termed ion selectivity, is a key feature of ion channels and forms the basis for their physiological function. Members of the degenerin/epithelial sodium channel (DEG/ENaC) superfamily of trimeric ion channels are typically sodium selective, but to a surprisingly variable degree. While acid-sensing ion channels (ASICs) are weakly sodium selective (sodium:potassium ratio ∼10:1), ENaCs show a remarkably high preference for sodium over potassium (>500:1). This discrepancy may be expected to originate from differences in the pore-lining second transmembrane segment (M2). However, these show a relatively high degree of sequence conservation between ASICs and ENaCs, and previous functional and structural studies could not unequivocally establish that differences in M2 alone can account for the disparate degrees of ion selectivity. By contrast, surprisingly little is known about the contributions of the first transmembrane segment (M1) and the preceding pre-M1 region. In this study, we used conventional and noncanonical amino acid–based mutagenesis in combination with a variety of electrophysiological approaches to show that the pre-M1 and M1 regions of mASIC1a channels are major determinants of ion selectivity. Mutational investigations of the corresponding regions in hENaC show that these regions contribute less to ion selectivity, despite affecting ion conductance. In conclusion, our work suggests that the remarkably different degrees of sodium selectivity in ASICs and ENaCs are achieved through different mechanisms. These results further highlight how M1 and pre-M1 are likely to differentially affect pore structure in these related channels.

Introduction

Acid-sensing ion channels (ASICs) and epithelial sodium channels (ENaCs) are members of the degenerin (DEG)/ENaC superfamily of trimeric ion channels and play important roles in neurotransmission and salt homeostasis, respectively. The six human ASIC isoforms known to date (1a, 1b, 2a, 2b, 3, and 4) can form homo- or heterotrimeric proton-gated ion channels and are found primarily in the nervous system, where they contribute to the depolarization of post-synaptic neurons. They are implicated in numerous physiological and pathophysiological processes, including in nociception (Chen et al., 2002; Duan et al., 2007; Mazzuca et al., 2007), learning and memory (Wemmie et al., 2002), fear (Ziemann et al., 2009), and neuronal death in ischemic stroke (Wang et al., 2015; Xiong and Xu, 2012). ENaCs comprise a family of related channels formed by three homologous subunits, α/δ, β, and γ, but the canonical channel formed by the α, β, and γ subunits is the most physiologically understood isoform (Haerteis et al., 2009). Canonical ENaCs are located in the apical membrane of epithelial cells, particularly in the kidney, colon, and lung, where they contribute to the control of body electrolyte and water homeostasis as well as the volume and composition of lung epithelial lining liquid, respectively (Hanukoglu and Hanukoglu, 2016; Rossier et al., 2015).

Both ASICs and ENaCs are voltage-insensitive channels and share a similar overall subunit topology with intracellular N- and C-termini, two membrane-spanning helices (M1 and M2), and a large extracellular domain (Cheng et al., 2018; Hanukoglu and Hanukoglu, 2016). They are inhibited by amiloride and contain sodium-selective pore modules, although the degree of Na^+/K^+ permeability greatly varies from ∼10:1 in ASICs (Lingueglia et al., 1997) to >500:1 in ENaCs (Kashlan and Kleyman, 2011; Palmer, 1982). Functional and structural evidence suggests that in both channel types, the ion-conducting pore is lined by M2 (Jasti et al., 2007; Lynagh et al., 2017; Noreng et al., 2018; Schild et al., 1997). Interestingly, this is also the region that displays the highest level of sequence conservation between ASICs and ENaCs. As such, the molecular basis for the

[1]Department of Drug Design and Pharmacology, University of Copenhagen, Copenhagen, Denmark; [2]Nanion Technologies, Munich, Germany; [3]School of Natural and Environmental Sciences, Newcastle University, Newcastle upon Tyne, UK.

Correspondence to Stephan A. Pless: stephan.pless@sund.ku.dk; M. Althaus's present address is Department of Natural Sciences, Institute for Functional Gene Analytics, Bonn-Rhein-Sieg University of Applied Sciences, Rheinbach, Germany; T. Lynagh's present address is Sars International Centre for Marine Molecular Biology, University of Bergen, Bergen, Norway.

pronounced discrepancy in sodium selectivity between the two types of channels remains unclear. In fact, both channel types contain a highly conserved G/SXS motif situated roughly in the middle of the M2, which had been proposed to form a size-exclusion filter (Jasti et al., 2007; Kellenberger et al., 1999a; Palmer, 1985). Previous work indeed suggested that the selectivity filter of ENaCs is formed by the S of the G/SXS motif (Kellenberger et al., 1999a), and most ASIC structures available to date display a marked constriction at the level of this highly conserved M2 sequence feature (Baconguis et al., 2014; Yoder and Gouaux, 2020). However, we have recently shown that the ASIC GAS sequence is unlikely to make a major contribution to ion selectivity in ASIC1a and ASIC2a, while acidic side chains in the lower M2 appear to be more important (Lynagh et al., 2020; Lynagh et al., 2017). Additionally, the latest ASIC structures show that the lower pore is lined by a reentrant loop formed by side chains from the N-terminus (Yoder and Gouaux, 2020), and this pre-M1 region has previously been implicated in ion selectivity in ASICs (Coscoy et al., 1999; Pfister et al., 2006), ENaCs (Gründer et al., 1999; Kellenberger et al., 2005) and the related MEC-4/MEC-10 channel (Arnadóttir et al., 2011). Unlike for ASICs, we lack reliable structural information on the pore module of ENaCs, and mutations to conserved acidic side chains in the lower M2 did not have a major impact on ion selectivity (Yang and Palmer, 2018). Overall, most previous studies have focused primarily on M2 with regard to contributions to ion selectivity; yet, little is known about the contribution of other parts of the pore module, such as M1 and the preceding pre-M1 region. Here, we therefore set out to conduct a comparative analysis of the potential contribution of M1 and pre-M1 to ion selectivity in mouse ASIC1a (mASIC1a) and human ENaCs (hENaCs).

We employed a combination of site-directed mutagenesis and noncanonical amino acid (ncAA) incorporation in whole-cell, single-channel, and high-throughput electrophysiological recordings. Our data suggest that two aromatic residues in ASIC1a M1 play an important role in maintaining a ∼10-fold Na^+/K^+ permeability ratio. Removal of the bulk of these side chains resulted in a marked decrease in relative Na^+/K^+ and Na^+/Cs^+ permeability ratios, likely by enlarging the pore diameter. Additionally, single amino acid substitutions of multiple residues in ASIC1a pre-M1 abolish ion selectivity. In contrast, neither the M1 nor the pre-M1 side chains appear to be important for ion selectivity in hENaC, but single-channel recordings suggest that some side chains may play a role in ion conduction. Together, our results reveal important yet different roles of the M1 and pre-M1 segments in ASICs and ENaCs, possibly due to differences in their lower pore structures. This consolidates the notion of fundamentally different mechanisms by which these related channel types achieve sodium selectivity.

Materials and methods

Chemicals

NaCl, $MgCl_2$, KCl, $BaCl_2$, CsCl, HEPES, EGTA, D-glucose, amiloride hydrochloride hydrate >98%, methylammonium chloride, dimethylamine hydrochloride, ethylammonium chloride, diethylamine hydrochloride, triethylammonium chloride, tetraethylammonium, propylamine hydrochloride, and tetrapropylammonium chloride were purchased from Sigma-Aldrich. Dipropylamine hydrochloride was purchased from TCI Chemicals.

Molecular biology

mASIC1a cDNA, cloned between the BamHI and SacI restriction sites of the pSP64 vector, was a gift from Dr. Marcelo Carattino (University of Pittsburgh, Pittsburgh, PA). hENaC α, β, and γ subunits in the pTNT vector were a gift from Dr. Diego Alvarez de la Rosa (University of La Laguna, San Cristóbal de La Laguna, Spain). The α subunit contained the T334 and A663 polymorphisms. The construct referred to as WT hENaC contains C-terminal truncations in the β and γ subunits (β_R566STOP and γ_K576STOP) to increase expression. Site-directed mutagenesis was performed using custom-designed primers (Eurofins Genomics) and regular PCR with *Pfu*Ultra II Fusion HS DNA Polymerase (Agilent Technologies). Plasmids were linearized with EcoRI (for mASIC1a) and BamHI (for hENaC) and used as a template for synthesis of mRNA with the Ambion mMESSAGE mMACHINE SP6 Transcription Kit (Thermo Fisher Scientific). ENaCα-mASIC1aM1 chimera DNA cloned between the NheI and Xhol restriction sites in the pUNIV vector was purchased from Twist Bioscience.

Incorporation of the ncAA naphthalene

The nitroveratryloxycarbonyl-protected ncAA naphthalene esterified with 5′-O-phosphoryl-2′-deoxycytidylyl-(3′→5′)adenosine was incorporated via the nonsense suppression method (Dougherty and Van Arnam, 2014). Modified *Tetrahymena thermophila* tRNA was prepared by annealing full-length 5′ and 3′ DNA strands (Integrated DNA Technologies); RNA was synthetized using the T7-Scribe transcription kit (CELLSCRIPT) and purified with Chroma Spin DEPC-H_2O columns (Clontech). The ncAA naphthalene was ligated to the tRNA with T4 DNA ligase (New England Biolabs). The aminoacylated tRNA was purified with phenol-chloroform extraction and ethanol purification, air dried, and stored at −80°C until use. The pellet was resuspended in 1 µl water and deprotected with 400-W UV light (Newport UV lamp [66921], including Newport power supply [69920]) immediately before injection into oocytes. The deprotected aminoacylated tRNA was mixed 1:1 with mASIC1a mRNA containing a TAG codon at position 50 and injected into oocytes.

Oocyte preparation and mRNA injection

Stage IV oocytes were extracted from female *Xenopus laevis* frogs (anesthetized in 0.3% tricaine under license 2014-15-0201-00031, approved by the Danish Veterinary and Food Administration) by surgery and washed thoroughly in OR-2 medium (in mM: 2.5 NaCl, 2 KCl, 1 $MgCl_2$, and 5 HEPES, pH 7.4). The oocytes were digested with type I collagenase (1.5 mg/ml; Roche) in OR-2. Stage V and VI oocytes were manually isolated and stored in OR-2 medium. For the injection, oocytes were lined up in a 35-mm dish containing OR-2. For the microinjection, glass capillaries (1.14 mm, 3.5 in; World Precision Instruments) were pulled using a horizontal puller (P-1000; Sutter Instruments)

and filled with mineral oil (Sigma-Aldrich). The tips of the capillaries were broken with fine tweezers to allow RNA uptake. RNA was injected into the oocytes at the oocyte equator (Nanoliter 2010 Injector; World Precision Instruments). RNA was injected in amounts as mentioned in the relevant figure legends, and oocytes were incubated in OR-3 medium (Leibovitz's L-15 Medium [Gibco] supplemented with 3 mM L-glutamine [Gibco], 0.25 mg/ml gentamicin [Gibco], 15 mM HEPES, pH 7.6) for 1–5 d at 18°C. For ENaC single-channel experiments, ovary lobes were purchased from the European *Xenopus* Resource Centre, and procedures were approved by the Animal Welfare and Ethical Review Body at Newcastle University (project identifier 630). RNA-injected oocytes were incubated at 16°C in a low-sodium solution as previously described (Wichmann et al., 2019).

Electrophysiological experiments and data analysis

For measurements of macroscopic currents through ASICs, oocytes were placed in a custom-built chamber (Dahan et al., 2004), through which bath solution (in mM: 96 NaCl, 2 KCl, 1.8 $BaCl_2$, and 5 HEPES, pH 7.6, with NaOH) was continuously perfused. For determination of pH concentration–response relationships, the extracellular solution (ECS) was rapidly and progressively switched to one with lower pH using a gravity-driven ValveBank8 system (AutoMate Scientific). The conditioning pH was 7.6, and, after each activating pulse, channels were allowed to recover for 1 min at pH 7.6. Cells were clamped at −20 mV (unless stated otherwise), and currents were recorded with microelectrodes filled with 3 mM KCl (pipette resistance <1 MΩ), OC-725C amplifier (Warner Instruments), and Digidata 1550 digitizer (Molecular Devices) at 1 kHz with 200-Hz filtering. The pH of half-maximal activation (pH_{50}) values were calculated with the four-parameter Hill equation in Prism 6 (GraphPad). For ion selectivity measurements in mASIC1a constructs, I-V relationships were determined at a holding potential of −60 mV and applying a 200-ms voltage ramp from −60 to 60 mV during the peak current. For determination of ion selectivity, reversal potentials with 96 mM extracellular Na^+, K^+, Li^+, and Cs^+, respectively, were determined using this voltage-ramp protocol. Ion permeability ratios were calculated using the measured reversal potentials and a version of the Goldman-Hodgkin-Katz equation (Eq. 1). The pH of the solutions was adjusted using the hydroxide of the respective ions (e.g., NaOH).

$$P_K/P_{Na} = \exp[F(V_{rev,Na}-V_{rev,K})]/RT \quad (1)$$

where F is Faraday's constant, R is gas constant, and T = 294 K.

For ion selectivity measurements in hENaC constructs, WT or mutant α, β, and γ subunits were injected in a 1:1:1 ratio with a final amount of 5–15 ng mRNA. For constructs that showed small macroscopic current sizes, the total RNA amount was increased to 50 ng. Oocytes injected with ENaC constructs were incubated in the presence of 100 µM amiloride to avoid cell death due to excess Na^+ uptake. For ion selectivity measurements, cells were continuously perfused with bath solution (in mM: 96 XCl, 2 $MgCl_2$, 1.8 $CaCl_2$, and 5 HEPES; "X" represents Na, K, Li, or Cs) containing 100 µM amiloride. Currents were elicited upon switching the solution to one without amiloride. After 1 min, when the currents had reached a steady-state level, a 1-s voltage step protocol was applied, ranging from −140 mV to 40 mV. To determine the amiloride-sensitive current, the protocol was repeated in the presence of 100 µM amiloride. Relative ion permeability ratios were calculated as relative amiloride-sensitive current amplitudes at −100 mV. Data were analyzed in Clampfit 10.7.

Statistical analysis was performed using GraphPad Prism version 7.0 software. An unpaired *t* test was used to compare two groups. Multiple groups were compared by one-way ANOVA with Dunnett's multiple comparisons test for comparison with a control group (WT). A P value <0.05 was considered significant. All bars and data points are presented as mean ± SD.

For cell-attached patch-clamp experiments, *Xenopus* oocytes were injected with 10–50 ng mRNA. After 24–48 h, the oocytes were mechanically devitellinized and placed in a recording chamber containing bath solution (in mM: 145 KCl, 1.8 $CaCl_2$, 10 HEPES, 2 $MgCl_2$, and 5.5 glucose at pH 7.4 adjusted with KOH). Patch pipettes were pulled from borosilicate glass capillaries (6–11 MΩ), heat polished, and filled with pipette solution (in mM: 145 NaCl, 1.8 $CaCl_2$, 10 HEPES, 2 $MgCl_2$, and 5.5 glucose). The pH of the pipette solution was adjusted with HCl and NaOH. Current signals were amplified using an LM-PC patch-clamp amplifier (List-Medical), low-pass filtered at 100 Hz (Frequency Devices), and recorded at 2 kHz with Axon Clampex software (Axon Instruments) using an Axon 1200 interface amplifier. Single-channel analysis was performed with Clampfit version 10.7 (Axon Instruments). Recordings were performed at room temperature. Single-channel amplitudes were plotted as a function of voltage and fitted to a linear curve, and values for slope conductances were determined.

Statistical analysis was performed using GraphPad Prism version 7.0 software. To compare two groups, an unpaired *t* test was used. Multiple groups were compared by one-way ANOVA with Dunnett's multiple comparisons test for comparing a control group (WT). A P value <0.05 was considered significant. All bars and data points are presented as mean ± SD.

Cell culturing and transfection of HEK293-T for automated patch-clamp recordings

ASIC1a knockout HEK293-T cells (provided by Dr. Nina Braun; Borg et al., 2020) were grown in monolayers in T75 and T175 flasks (Orange Scientific) in cDMEM (Gibco DMEM supplemented with 10% FBS [Thermo Fisher Scientific] and 1% penicillin-streptomycin [Thermo Fisher Scientific]) and incubated at 37°C in a humidified 5% CO_2 atmosphere. Cells were split at near confluency by treatment with trypsin-EDTA (Thermo Fisher Scientific) after the cells were washed with PBS. Cells were counted with an EVE automatic cell counter (NanoEntek) and seeded into 10-cm dishes (Orange Scientific) at a density of 2.0×10^6 cells/dish.

For transient transfections in 10-cm dishes, 7 µg of DNA was mixed with 21 µl of Trans-IT LT1 transfection reagent (Mirus Bio) or LipoD transfection reagent and 1,750 µl DMEM and incubated at room temperature for 20 min to allow formation of DNA–transfection reagent complexes before addition to the cells. Transfected cells were incubated for 24 h.

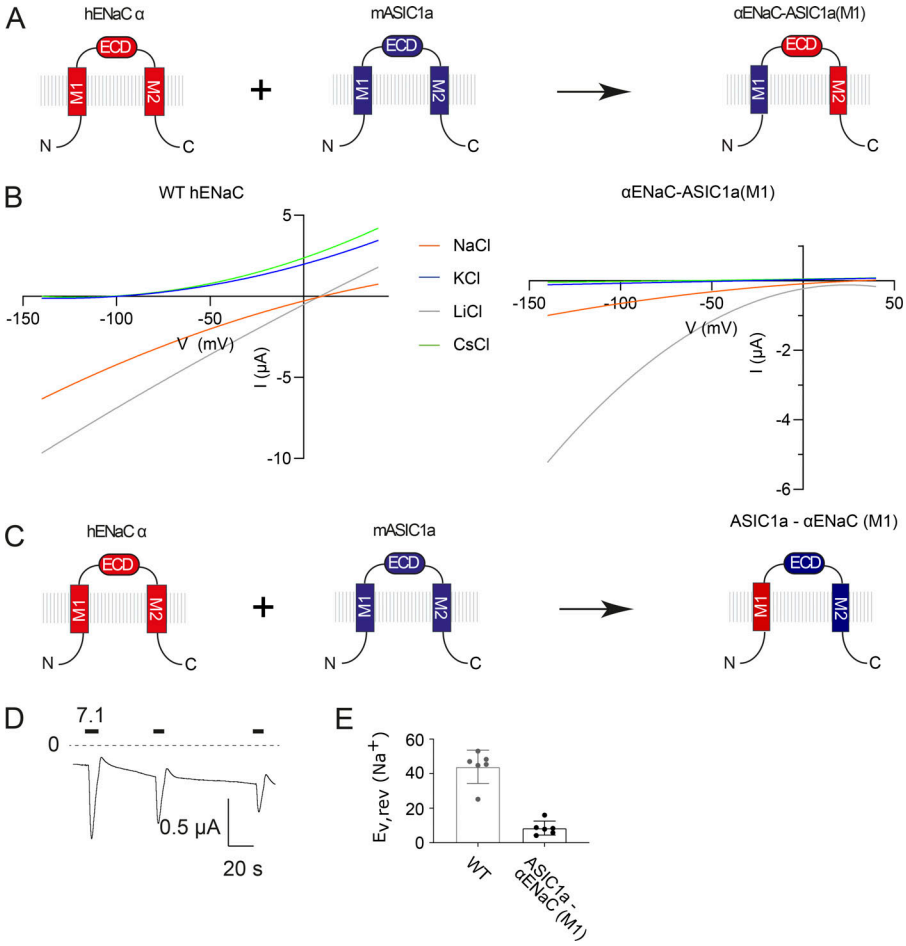

Figure 1. **M1 chimeras suggest an indirect role for M1 in selectivity. (A)** Cartoon illustration of hENaC-mASIC1a chimera design and amiloride-sensitive currents with Na^+ as the primary extracellular cation. **(B)** I-V relationships of WT hENaC and hENaC containing the M1 segment of mASIC1a in the α subunit, αENaC-ASIC1a(M1). **(C)** Cartoon illustration of mASIC1a-hENaC chimera. **(D)** Current traces of mASIC1a containing the M1 segment of hENaC α, ASIC1a-αEnaC(M1). Cells were continuously perfused in ND96 solution (pH 8), and channels were activated with pH 7.1. **(E)** Reversal potentials with extracellular 96 mM NaCl determined for WT mASIC1a and ASIC1a-αENaC(M1) using a 200-ms voltage ramp from −60 to +60 mV during the peak current. Currents during the voltage ramps at pH 7.4 were subtracted from currents during activating pH (pH 6). $E_{v,rev}$, reversal potential.

Transfected cells were harvested by trypsin-EDTA treatment (2 ml/10-cm dish). Detached cells were resuspended in DMEM and centrifuged at 2,000 *g* for 2 min. The cells were resuspended in a 1:1 mixture of DMEM and Nanion Technologies physiological solution (in mM: 140 NaCl, 4 KCl, 1 $MgCl_2$, 2 $CaCl_2$, 10 HEPES, and 5 glucose, pH 7.4). Automated patch-clamp experiments were performed 24 h after transfection.

Automated patch-clamp recordings

The permeability of ASIC1a to a range of monovalent cations (MA^+, methylammonium$^+$; DMA^+, dimethylamine$^+$; EA^+, ethylamine$^+$; DEA, diethylamine$^+$; TEA, triethylamine$^+$; $TetraEA^+$, tetraethylamine$^+$; PA^+, propylamine$^+$; DPA^+, dipropylamine$^+$; and $TetraPA^+$, tetrapropylamine) different in size and shape was assessed with automated whole-cell patch clamping on the SynchroPatch 384PE. The experiment was designed such that the intracellular solution (ICS) contained only cations impermeable (or with very low permeability) for ASIC1a, whereas the ECSs contained one of a range of test ions. Solutions used for the automated patch-clamp experiment were as follows: ECS: 140 mM XCl, 4 mM CsCl, 1 mM $MgCl_2$, 2 mM $BaCl_2$, 10 mM HEPES pH 7.4 and 6, 290 mosmol/kg; ICS: 80 mM $NMDG_2$-SO_4, 20 mM CsCl, 10 mM HEPES pH 7.2, 270 mosmol/kg.

The SynchroPatch 394PE consists of a Biomek FX^P liquid-handling station (Beckman Coulter) and a planar patch-clamp module (Nanion Technologies), which can be controlled simultaneously via a computer terminal using the PatchControl384 and Biomek software (version 4.1). 25 ml of cells expressing hASIC1a WT or hASIC1a F50A (>4.0 × 10^6 cells) were loaded into a Teflon reservoir. Cells were incubated at 20°C and shaken at 200 rpm in the integrated cell compartment of the SynchroPatch 384PE.

For patch-clamp recordings, 15 µl of cells were loaded into each well of an NPC-384 medium-resistance single-hole plate (Nanion Technologies). The plate contains 384 individual wells with a single patch-clamp orifice where the cells and ECSs are delivered. The design of the plate and the patch-clamp module allows perfusion of the ICS during an experiment. Cells were caught on the patch-clamp holes by applying a brief pressure of −100 mbar, and another pulse of pressure (−150 mbar) was applied to reach whole-cell configuration. Cells were clamped at 0 mV under atmospheric pressure. Seals of 50 MΩ and above were included in the analysis.

ECSs were provided in 12-well Teflon reservoirs, with each column of wells containing an ECS with 140 mM of one of the following cations provided as chloride salts shown in Fig. 1 C. One 12-well dish contained ECSs with resting pH (7.4), and another dish contained ECSs with activating pH (pH 6). ECSs were applied using a liquid stacking approach as described elsewhere (Braun et al., 2021 *Preprint*). The pipette tips were loaded with 25 µl pH 7.4 solution followed by 15 µl pH 6.0 solution. For determination of I-V relationships, four sweeps were recorded. For

each sweep, the baseline current was recorded for 1 s (clamped at 0 mV) before the application of the activating solution, followed by a delayed dispersion with the pH 7.4 solution. This was followed by two washing steps with pH 7.4 solution, after which the protocol was repeated at a different voltage.

Online supplemental material

Fig. S1 contains sequence logos for M1 and M2, along with an overview of the nonsense suppression method. Fig. S4 shows current traces and a plot of ion selectivity versus pH_{50} of mASIC1a M1 mutants. Fig. S5 illustrates the underlying principle and data averages for automated patch-clamp recordings. Figs. S2, S3, and S6 show sequence alignments. Fig. S7 shows chicken ASIC1 (cASIC1) structures and current traces for selected mASIC1a pre-M1 mutants.

Results

M1-swapped chimeras show altered function

Unlike the highly conserved protein sequences of the pore-lining M2 segments of ASICs and ENaCs, there is noticeable sequence divergence in the M1 segments (Fig. S1, A and B; see Figs. S2 and S3 for further information). We hypothesized that differences in the M1 segments between the two channel types may partially account for the observed difference in Na^+/K^+ selectivity. To directly test this notion, we swapped the M1 segment of mASIC1a with that of the hENaC α subunit and vice versa (residues A44–F69 in mASIC1a and the equivalent residues in hENaC α) and expressed the resulting chimeras in *Xenopus* oocytes. The αENaC–ASIC1a (M1) chimeric construct, when coexpressed with WT hENaC β and γ, yielded amiloride-sensitive currents (Fig. 1, A and B) but required injection of 100 ng RNA and 3 d of incubation for detection of currents. Notably, the αENaC-ASIC1a (M1) construct appeared to be inwardly rectifying. Although the small current magnitudes carried by K^+ and Cs^+ prevented us from accurately determining the effects of the M1 swap, the data tentatively suggest an increased permeability for K^+ and Cs^+ (I_{K+}/I_{Na^+} = 0.09 ± 0.06 and I_{Cs+}/I_{Na^+} = 0.10 ± 0.10 at −100 mV). By contrast, the Li^+/Na^+ amiloride-sensitive current ratio was markedly increased (I_{Li}/I_{Na} = 4.2 ± 0.06 compared with 1.2 ± 0.19 in WT hENaC at −100 mV).

The ASIC1a–αENaC (M1) chimera formed constitutively active, pH-sensitive channels that underwent severe tachyphylaxis, rendering an accurate analysis of relative ion permeability ratios of this construct infeasible (Fig. 1, C and D). However, the measured reversal potential with Na^+ as the primary cation in the ECS was markedly reduced compared with WT mASIC1a, suggesting that the M1 swap reduces Na^+ selectivity (Fig. 1 E).

The altered function of these M1-swapped chimeras suggests that the M1 region contributes to ion selectivity in both channel types. This prompted us to investigate the role of M1 side chains in further detail.

Residue swapping in the variable region of M1 does not affect ion selectivity of mASIC1a

Because pronounced tachyphylaxis precluded obtaining detailed information on relative ion permeabilities of the mASIC1a-hαENaC(M1) chimera, we resorted to swapping nonconserved amino acids in the M1 segment of mASIC1a, one at a time, with those found at corresponding positions in hENaC-α (highlighted in red in Fig. 2 A). We expressed WT or mutant channels in *Xenopus* oocytes and determined ion selectivity by measuring relative ion permeabilities of Na^+, Li^+, K^+, and Cs^+. Mutations in the more variable region of M1 (residues C3′L and G6′C-Q20′G) had minimal effects on relative ion permeability ratios (Fig. 2 C, Fig. S4, and Table 1), suggesting that these residues do not play critical roles in ion selection in mASIC1a.

Substitution of aromatic residues in the lower M1 region of mASIC1a affects ion selectivity

Next, we tested the possibility that bulky aromatic side chains in the M1 segments are important in maintaining the structural integrity and/or size of the pore of mASIC1a (highlighted in blue, Fig. 2 A). We found that substitutions of W0′ and F4′ altered ion selectivity markedly and decreased functional expression, particularly for the W0′ position (Fig. 2 C and Tables 1 and 2). Decreasing the side chain volume of W0′ to F or L reduced the Na^+/K^+ permeability ratio to unity, caused an alkaline shift in the pH_{50}, decreased the rate of desensitization, and induced a constitutive current component (Fig. S4), whereas incorporation of the slightly bulkier ncAA naphthalene with the in vivo nonsense suppression method (Fig. S1 C) did not increase ion selectivity but resulted in an alkaline shift in the pH_{50} and increased the rate of desensitization (Fig. S4). Thus, the bulk of W0′ appears important for both ion selectivity and gating (Fig. 2, B and C; Table 2; and Fig. S4). Substitution of F4′ for smaller side chains (L and A) reduced ion selectivity, but increasing the bulk with a W mutation or incorporation of naphthalene did not increase ion selectivity (Table 2). Contrary to expectations, the relative Na^+/Cs^+ permeability ratio was significantly reduced in F4′Nap compared with WT. This was not investigated further. None of the F4′ mutants affected the pH_{50} (Fig. 2 C and Table 2). Hence, the F4′ mutants do not affect gating, but decreasing the bulk of the side chain appears to be detrimental to ion selectivity. Substitution of the aromatic residues in the upper M1 (Y21′E-F23′A) did not affect ion selectivity or proton sensitivity, although the role of the Y22′A mutant could not be deciphered due to lack of current. In light of the available toxin-stabilized open structure of cASIC1, the lower pore is too wide for the W0′ and F4′ side chains to contribute to ion permeation (Fig. S7 A). However, according to the latest cASIC1 structure in the desensitized state, both W0′ and F4′ are interacting with lower pore-forming residues (Fig. S7 B). In this structure, the absolutely conserved W0′ is making contacts both with a reentrant loop that forms the lower pore of the channel according to this structure and with residues in the neighboring M2 helix (Fig. S7 B). This complements our data showing that F4′ is important for ion selectivity, whereas the absolutely conserved W0′ is critical for both ion selectivity and gating (Fig. 2 C and Table 2).

Permeability properties of WT ASIC1a and the nonselective F4′A mutant

To test the hypothesis that the removal of side chain bulk of aromatic residues in the lower ASIC1a M1 affects the size of the pore, we set out to measure currents carried by a range of

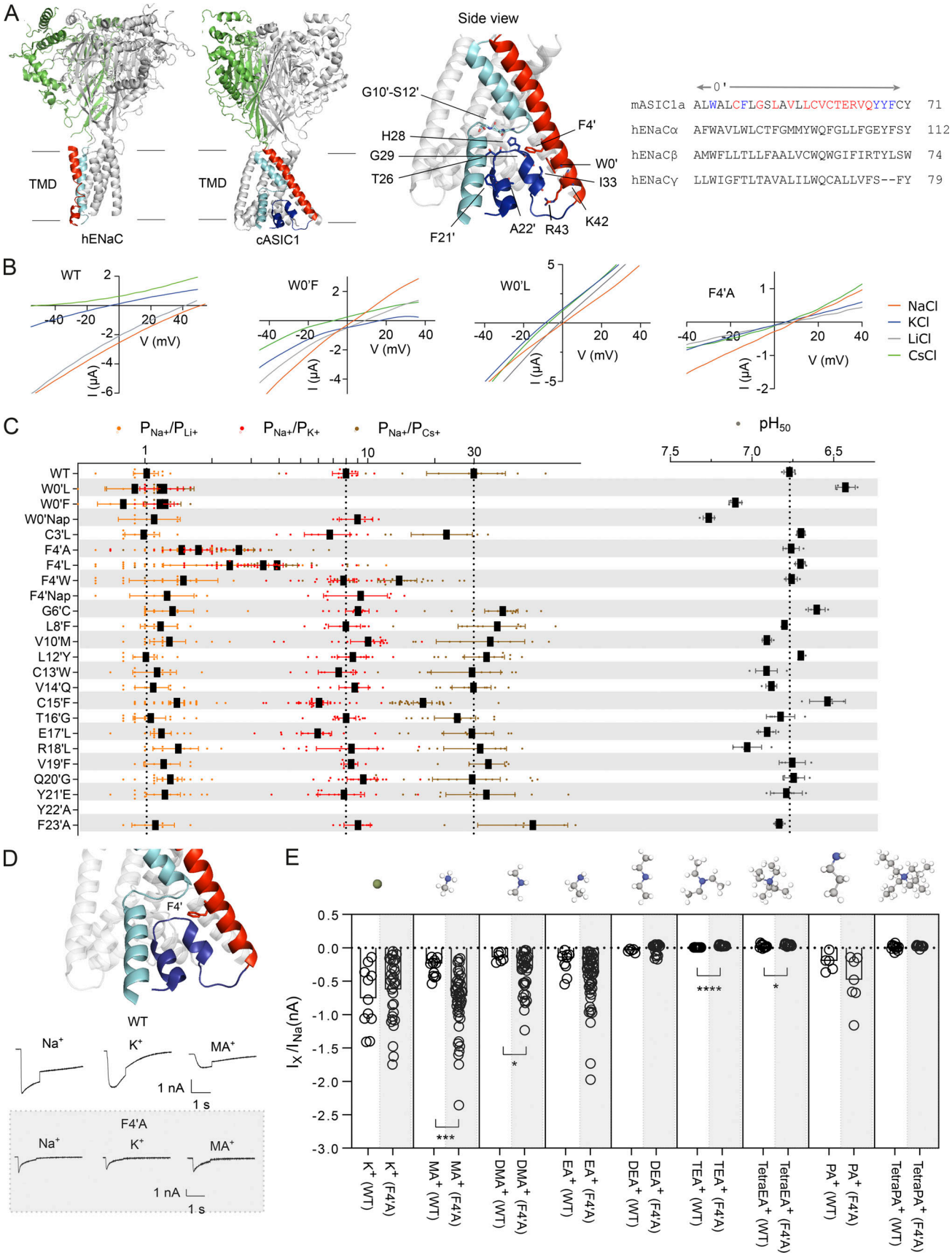

Figure 2. **M1 side chains contribute to ion selectivity in mASIC1a. (A)** hENaC (Protein Data Bank accession no. 6BQN) and cASIC1 (Protein Data Bank accession no. 6VTK) structures (left panel), close-up of cASIC1 structure (middle panel), and sequence alignment of mASI1a and hENaC α, β, and γ M1 (right

panel). The residues that were substituted individually for the equivalent residue in hENaC α are shown in red, and all aromatics mutated are shown in blue. Transmembrane domains are indicated by "TMD" labels. **(B)** I-V relationships for WT mASIC1a and selected nonselective mASIC1a mutants. **(C)** Relative ion permeabilities and pH_{50} values for mASIC M1 mutants. Data are shown as individual data points and mean ± SD. **(D)** Upper panel shows a close-up view of cASIC1 F4′ (Protein Data Bank accession no. 6VTK; M1, red; M2, cyan; pre-M1, dark purple) and example traces of peak current amplitudes at −20 mV of WT hASIC1a and the nonselective F4′A mutant with different extracellular monovalent cations (lower panel). The solutions containing the different monovalent cations were applied using a liquid stacking approach as described elsewhere (Braun et al., 2021 *Preprint*). **(E)** Currents measured in HEK293-T cells using a high-throughput patch-clamp robot (SynchroPatch; Nanion Technologies). Currents carried by the test ions were compared with those carried by Na^+ using an unpaired *t* test. Note that we cannot exclude the possibility that the absence of permeant ions in the internal solution of SynchroPatch experiments may affect pore structure and cause the lower degree of Na^+/K^+ selectivity. Data are shown as individual data points and mean ± SD. *, P < 0.05; ***, P < 0.001; ****, P < 0.0001. ICS in mM: 80 NMDG-SO_4, 20 CsCl, and 10 HEPES, pH 7.2. ECS in mM: 140 test ion, 4 CsCl, 1 $MgCl_2$, and 10 HEPES, pH 7.4 or pH 6, respectively.

monovalent cations with different sizes through WT and the nonselective F4′A mutant. We chose the F4′A mutant because it produced larger currents in *Xenopus* oocytes and because it does not obviously affect channel gating (unlike W0′F and W0′L). HEK293T cells without endogenous hASIC1a channels (Borg et al., 2020) were transfected with WT or F4′A hASIC1a DNA, and currents were recorded using an automated patch-clamp system (SyncroPatch 384PE). Similar to conventional patch clamping, the SyncroPatch 384PE system allows control over both the ICS and the ECS, but with greater overall throughput. We used *N*-methyl-D-glucamine ($NMDG^+$) as the only cation in the ICS to ensure minimal outward ionic flow from the ICS and thus to facilitate isolation of small inward currents carried by the extracellular test ions. pH 6–induced currents were recorded at four test potentials (−20, 10, 40, and 70 mV) to estimate the reversal potentials with different extracellular monovalent test ions (Fig. S5). Fig. 2 E shows the pH 6–induced inward currents at −20 mV carried by the different monovalent test ions normalized to the current carried by Na^+. Based on these data, the F4′A mutant conducts larger monovalent cations more readily than WT hASIC1a (Fig. 1 E and Table 3). For example, the current carried by MA^+ in F4′A is almost equal in magnitude to the current carried by Na^+ (I_{MA}/I_{Na} = 0.81 ± 0.45; P = 0.29), whereas in WT, the magnitude of the MA^+ current is only one-third of the Na^+ current (I_{MA+}/I_{Na^+} = 0.31 ± 0.14; P < 0.001; Fig. 2, D and E). Also, the permeability of DMA^+ is significantly increased in F4′A (I_{DMA+}/I_{Na^+} = 0.40 ± 0.31) compared with WT (I_{DMA+}/I_{Na^+} = 0.14 ± 0.07; P < 0.05). A similar pattern was observed when we examined the reversal potentials with the respective extracellular test ions. Fig. S5 C shows reversal potentials estimated with different monovalent cations. The corresponding relative ion permeability ratios are reduced in the F4′A mutant for all ions except for EA^+ (Fig. S5 D). This suggests that the pore of the F4′A mutant is larger than that of the WT channel.

Table 1. **Amiloride-sensitive currents with extracellular Na^+ of hENaC WT and designated mutants**

Construct	I_{Na+} (μA)
hENaC WT	−12.3 ± 4.4
α(W0′F)βγ	−2.1 ± 0.4[a]
α(W0′F)β(W0′F)γ	−0.7 ± 0.4[a]
α(W0′F)β(W0′F)γ(W0′F)	n.d.
α(W4′A)βγ	−5.7 ± 2.6[b]
α(W4′A)β(T4′A)γ	−3.4 ± 1.7[b]
α(W4′A)β(T4′A)γ(T4′A)	−14.0 ± 5.3

Xenopus oocytes were injected with 5 ng RNA (hENaC WT, α(W4′A)βγ and α(W4′A)β(T4′A)γ) or 50 ng RNA (α(W0′F)βγ, α(W0′F)β(W0′F)γ, and α(W0′F)β(W0′F)γ(W0′F)) and incubated for 1–3 d. Values are presented as mean ± SD. n.d., not determined. Values for the mutants were compared with WT and analyzed using one-way ANOVA with Dunnett's multiple comparisons test.
[a]P < 0.0001.
[b]P < 0.01.

Our mASIC1a data show that substitution of the F4′ side chain significantly affects the size of the pore and increases the permeability toward larger monovalent cations. This finding supports the notion that F4′, and possibly W0′, can indirectly affect ion selectivity. Because aromatic residues at the 0′ positions are conserved in all three hENaC subunits and the 4′ residue in hENaC α is also an aromatic, we hypothesized that these residues in hENaC might play an equally important role in ion selectivity.

The 0′ and 4′ residues of hENaC M1 are unlikely to be critical for ion selectivity

Based on the mutational screen performed on the M1 segment of mASIC1a, we concluded that side chains at the 0′ and 4′ positions are important for ion selectivity. We therefore decided to investigate the role of the corresponding residues in hENaC. hENaC α, β, and γ subunits were expressed in *Xenopus* oocytes, and we measured currents using two-electrode voltage clamp. The voltage protocol and I-V relationships for WT hENaC and a designated mutant in either 96 mM NaCl, KCl, LiCl, or CsCl in the bath solution are shown in Fig. 3, A–C. For WT hENaC, we found that Na^+ and Li^+ currents reverse at ∼25 mV, whereas Cs^+ and K^+ are virtually nonpermeable, because the Cs^+ and K^+ currents reverse at a membrane potential of less than −100 mV. This is consistent with previously observed values for Na^+/K^+ and Na^+/Cs^+ current ratios (Palmer, 1982, 1990). Because reversal potentials could not be accurately determined, relative ion conductance ratios were estimated as amiloride-sensitive K^+, Li^+, and Cs^+ currents measured at −100 mV normalized to the amiloride-sensitive Na^+ current for all hENaC constructs (Kellenberger et al., 2001; Kellenberger et al., 1999a).

Single amino acid substitutions were introduced at the 0′ and 4′ positions in one, two, or all three hENaC subunits. W0′L or W0′A substitutions in hENaC α coexpressed with WT β and WT γ rendered the channel nonfunctional, but the W0′F mutation in hENaC α expressed with WT β and WT γ yielded amiloride-

Table 2. **pH_{50} values and relative ion permeability ratios for mASIC1a M1 substitutions**

Construct	pH_{50}	*n*	P_{Na+}/P_{K+}	P_{Na+}/P_{Li+}	P_{Na+}/P_{Cs+}	*n*
WT	6.8 ± 0.0	5	8.0 ± 1.6	1.0 ± 0.2	29.7 ± 17.2	11
W0′Nap	6.4 ± 0.1[a]	4	9.0 ± 1.7	1.1 ± 0.3	n.d.	5–7
W0′L	7.1 ± 0.0[a]	4	1.2 ± 0.3[a]	0.9 ± 0.2	1.2 ± 0.5[a]	6
W0′F	7.3 ± 0.0[a]	5	1.2 ± 0.2[a]	0.8 ± 0.2	1.2 ± 0.2[a]	6
C3′L	6.7 ± 0.0	5	6.8 ± 2.0	1.0 ± 0.2	22.6 ± 8.3	8–9
F4′A	6.8 ± 0.1	5	1.7 ± 0.6[a]	1.5 ± 0.7	2.6 ± 1.2[a]	30–33
F4′L	6.7 ± 0.0	5	3.4 ± 1.9[a]	2.4 ± 2.8[b]	3.9 ± 2.2[a]	24–25
F4′W	6.8 ± 0.0	5	7.8 ± 2.2	1.5 ± 1.5	13.8 ± 6.4[b]	23–24
F4′Nap	n.d.		9.3 ± 3.5	1.3 ± 0.4	n.d.	
G6′C	6.6 ± 0.1[c]	5	9.0 ± 1.8	1.3 ± 0.5	40.3 ± 11.4	13
L8′F	6.8 ± 0.0	5	8.0 ± 1.7	1.2 ± 0.3	38.1 ± 16.6	8–9
V10′M	6.9 ± 0.0[b]	5	10.0 ± 3.3	1.3 ± 0.4	35.6 ± 18.1	8–17
L12′Y	6.7 ± 0.0	5	8.6 ± 2.1	1.0 ± 0.2	34.1 ± 10.3	11–13
C13′W	6.9 ± 0.1[b]	7	7.4 ± 1.8	1.1 ± 0.3	29.3 ± 13.1	9
V14′Q	6.9 ± 0.0[d]	5	8.7 ± 1.7	1.1 ± 0.2	29.8 ± 7.7	9
C15′F	6.5 ± 0.1[a]	4	6.0 ± 1.6	1.4 ± 0.3	17.7 ± 4.8[d]	31–34
T16′G	6.8 ± 0.1	5	8.0 ± 1.3	1.1 ± 0.3	25.2 ± 7.9	12–13
E17′L	6.9 ± 0.1[b]	5	6.0 ± 1.8	1.2 ± 0.2	29.3 ± 10.4	10–16
R18′L	7.0 ± 0.1[a]	5	8.5 ± 3.8	1.4 ± 0.4	31.9 ± 12.0	8–11
V19′F	6.8 ± 0.1	4	8.4 ± 0.7	1.2 ± 0.3	34.8 ± 7.6	8
Q20′G	6.7 ± 0.1	5	9.5 ± 2.8	1.3 ± 0.3	29.4 ± 17.1	14–16
Y21′E	6.8 ± 0.1	5	7.8 ± 3.2	1.2 ± 0.4	34.1 ± 18.4	12–14
Y22′A	n.d.		n.d.	n.d.	n.d.	
F23′A	6.8 ± 0.0	5	9.0 ± 1.3	1.1 ± 0.3	55.0 ± 22.8	6–7

Values are presented as mean ± SD, and *n* refers to the number of oocytes tested; n.d., not determined. The Y22′A mutant did not produce proton-gated currents. Values for the mutants were compared with WT and analyzed using one-way ANOVA with Dunnett's multiple comparisons test.
[a]$P < 0.0001$.
[b]$P < 0.01$.
[c]$P < 0.001$.
[d]$P < 0.05$.

sensitive currents and showed relative amiloride-sensitive currents similar to WT hENaC (Fig. 3 E; see Table 4). W0′F substitutions in both α and β ENaC (expressed with WT γ) increased the amiloride-sensitive Li^+/Na^+ but had no significant effect on the K^+/Na^+ or Cs^+/Na^+ currents (Fig. 3 E and Table 4). With W0′F substitutions in all three hENaC subunits, amiloride-sensitive currents could not be determined with any of the four ions due to lack of current. Although we cannot comment on the triple-mutant scenario, W0′ does not appear to contribute to ion selectivity in hENaC, at least upon W0′ substitutions in one or two of the three subunits. Substitution of the amino acids at the 4′ position in α, β, and γ ENaC yielded measurable amiloride-sensitive currents for all three mutants, but the relative amiloride-sensitive current profiles of all tested 4′ position mutations are similar to that of WT hENaC (Fig. 3 E and Table 4).

Although mutations at the 0′ and 4′ positions of hENaC had no significant effect on ion selectivity, there is a possibility that other amino acids in M1 of hENaC contribute to ion selectivity. The M1 of hENaC contains a higher number of aromatic residues than mASIC1a (Fig. 1 A). We set out to test the hypothesis that the larger number of aromatic residues explains why hENaC is more Na^+ selective, possibly by indirectly decreasing the pore diameter. To this end, single amino acid substitutions were introduced individually into the M1 of hENaC. For positions that contained an aromatic amino acid in two or three subunits, substitutions were made in two or all three subunits. Fig. 3 E depicts amiloride-sensitive currents with Li^+, K^+, or Cs^+ relative to the current carried by Na^+. None of the mutants exhibited significantly altered ion selectivity profiles, and all remained nonpermeable to K^+ and Cs^+, except for α(F19′A)βγ and α(Y23′A)βγ, which showed a slight permeability for K^+ and Cs^+ (Fig. 3 E and Table 4). Some mutants exhibited modestly altered Li^+/Na^+ current. These include α(F19′A)βγ, α(Y22′A)βγ, and αβ(F22′A)γ (Fig. 3 E; see Table 4).

Table 3. **Normalized pH 6–induced inward peak currents carried by extracellular monovalent cations in hASIC1a WT and F4′A**

Test ion	I_x/I_{Na} (WT)	*n*	I_x/I_{Na} (F4′A)	*n*
K^+	0.8 ± 0.5	11	0.6 ± 0.5	32
MA^+	0.3 ± 0.1[a]	11	0.8 ± 0.5	46
DMA^+	0.1 ± 0.1[b]	6	0.4 ± 0.3	32
EA^+	0.2 ± 0.2	9	0.5 ± 0.4	47
DEA^+	0.04 ± 0.02	5	0.02 ± 0.08	18
TEA^+	−0.01 ± 0.0[c]	9	−0.03 ± 0.01	12
$TetraEA^+$	−0.02 ± 0.03[b]	11	−0.04 ± 0.02	12
PA^+	0.2 ± 0.1	5	0.5 ± 0.4	7
$TetraPA^+$	−0.01 ± 0.4	11	−0.02 ± 0.02	9

Currents were recorded on a high-throughput patch-clamp robot (SynchroPatch 384PE). Currents carried by the different test ions were normalized to the mean Na^+ current. Values are presented as mean ± SD. Currents carried by the test ions were compared with those carried by Na^+ using an unpaired *t* test.
[a]P < 0.001.
[b]P < 0.05.
[c]P < 0.0001.

Given that 0′ and 4′ mutations in mASIC1a alter channel gating, apparent pore diameter, and ion selectivity and that M1 aromatic residues are highly conserved (especially in ENaCs), we were surprised that 0′ and 4′ mutations in hENaC had no effect on ion selectivity (note that only the 4′ position in hENaC α is aromatic in nature, whereas 4′ is occupied by threonines in β and γ subunits). To further test the potential contributions of conserved 0′ and 4′ aromatic side chains to currents through hENaC, we measured single-channel conductance in WT and mutant channels. We expressed hENaC WT and 0′ and 4′ mutants in *Xenopus* oocytes and measured the single-channel conductances of WT and 0′/4′ mutants containing amino acid substitutions in one subunit (α) or two subunits (α and β). The single-channel conductances of the 0′ mutants were significantly increased from 4.7 ± 1.0 pS in WT hENaC to 7.4 ± 3.2 pS in α(W0′F)βγ and 8.6 pS ± 1.0 pS in α(W0′F)β(W0′F)γ (Fig. 2, F and G; and Table 5), whereas the single-channel conductances of the 4′ single and double mutants were not significantly different from WT hENaC (Fig. 3, F and G; and Table 5). These results implicate the highly conserved W0′ but not the 4′ side chain in conductance.

Our data show that although hENaC M1 mutations can affect conductance, their impact on ion selectivity is generally small. We thus conclude that M1 contributes to ion selectivity to a lesser degree in hENaC than in mASIC1a.

Determinants of ion selectivity in the pre-M1 segment of mASIC1a

We next wanted to expand our investigation into other regions possibly contributing to ion selectivity in ASICs and ENaCs. Because the most important determinants of ion selectivity in M1 were found to be located toward the intracellular end of M1, we wanted to probe side chains further upstream of these positions. Work by others had already highlighted the functional importance of this pre-M1 region (Coscoy et al., 1999; Pfister et al., 2006), and the latest cASIC structures reveal that residues in the N-terminus preceding M1 form part of the lower pore structure in ASICs (Yoder and Gouaux, 2020). We used comparative sequence analysis of 33 ASIC and ENaC sequences, as well as other members of the DEG/ENaC superfamily (Fig. 4 A and Fig. S6), to identify potentially important determinants of ion selectivity in the pre-M1 segment. The resulting sequence logo indicates the degree of amino acid conservation in this region (Fig. 4 A).

We started by investigating the N-terminal end of this sequence stretch, which in mASIC1a comprises a FASSST sequence motif: substitution of F21 (mASIC1a numbering) for the smaller L or A reduced relative ion permeability to unity and caused an alkaline shift in the proton sensitivity (pH_{50} 6.8 ± 0.0 in WT, 7.0 ± 0.0 in F21A, and 7.0 ± 0.1 in F21L), whereas substitution with the larger W decreased ion selectivity to a lesser degree but caused a similar alkaline shift in pH_{50} (7.1 ± 0.1; Fig. 4 C and Table 6). Substitution of the neighboring A22 for G and L also abolished ion selectivity and shifted the pH_{50} values to 7.1 ± 0.0 in A22G and 7.1 ± 0.0 in A22L. The S23A, S23E, and S24A mutants were not significantly different from WT in terms of ion selectivity or the pH_{50} values, but the S24E mutant exhibited a modest increase in the Na^+/K^+ permeability ratio (10.7 ± 3.9). Previous work had suggested hASIC1a S25 to be phosphorylated (Duan et al., 2012), so we mutated S25 to A and E in order to either remove a potential phosphorylation (A) or mimic the negative charge of a phosphate group (E). However, Na^+ selectivity in S25A was only slightly decreased compared with WT ($P_{Na+/K+}$ permeability = 5.6 ± 1.6, with WT-like proton sensitivity: pH_{50} 6.8 ± 0.1), while the S25E mutant abolished Na^+ selectivity and proton sensitivity was markedly increased (pH_{50} 7.1 ± 0.1). This argues against a direct role for phosphorylation of S25 in channel function. By contrast, substitution of the neighboring T26 for C, V, or E reduced ion selectivity to unity and drastically shifted the pH_{50} to more alkaline pH (Fig. 4, B and C; and Table 6), while the T26S ion selectivity profile resembled that of WT. For this mutant, the pH_{50} value was not different from WT, and it displayed only modest differences in the Na^+/K^+ permeability ratio (5.7 ± 1.8 compared with 6.8 ± 0.3 in WT) and in the Na^+/Cs^+ permeability ratio (9.7 ± 1.7 compared with 6.8 ± 0.3 in WT; Fig. 3 C and Table 6). Together, this indicates that the T26 hydroxyl (or its T26S equivalent) is crucial to both Na^+ selectivity and proton-dependent gating. However, we found that the isosteric T26V mutant did not alter the amplitude of Na^+-mediated single-channel currents, suggesting that the loss of selectivity in this mutant does not reduce relative permeability of Na^+, but is rather more likely to increase relative permeability of K^+ (Fig. 4, D and E).

The highly conserved H28 and G29 positions were recently shown to be located near the apex of a reentrant loop formed by part of the cASIC1 N-terminus (Yoder and Gouaux, 2020). Consistent with the notion that both residues are crucial to function (and lining the permeation pathway), mutations at both sites disrupted ion selectivity and proton sensitivity: substitution of either of the two amino acids with A resulted in channels

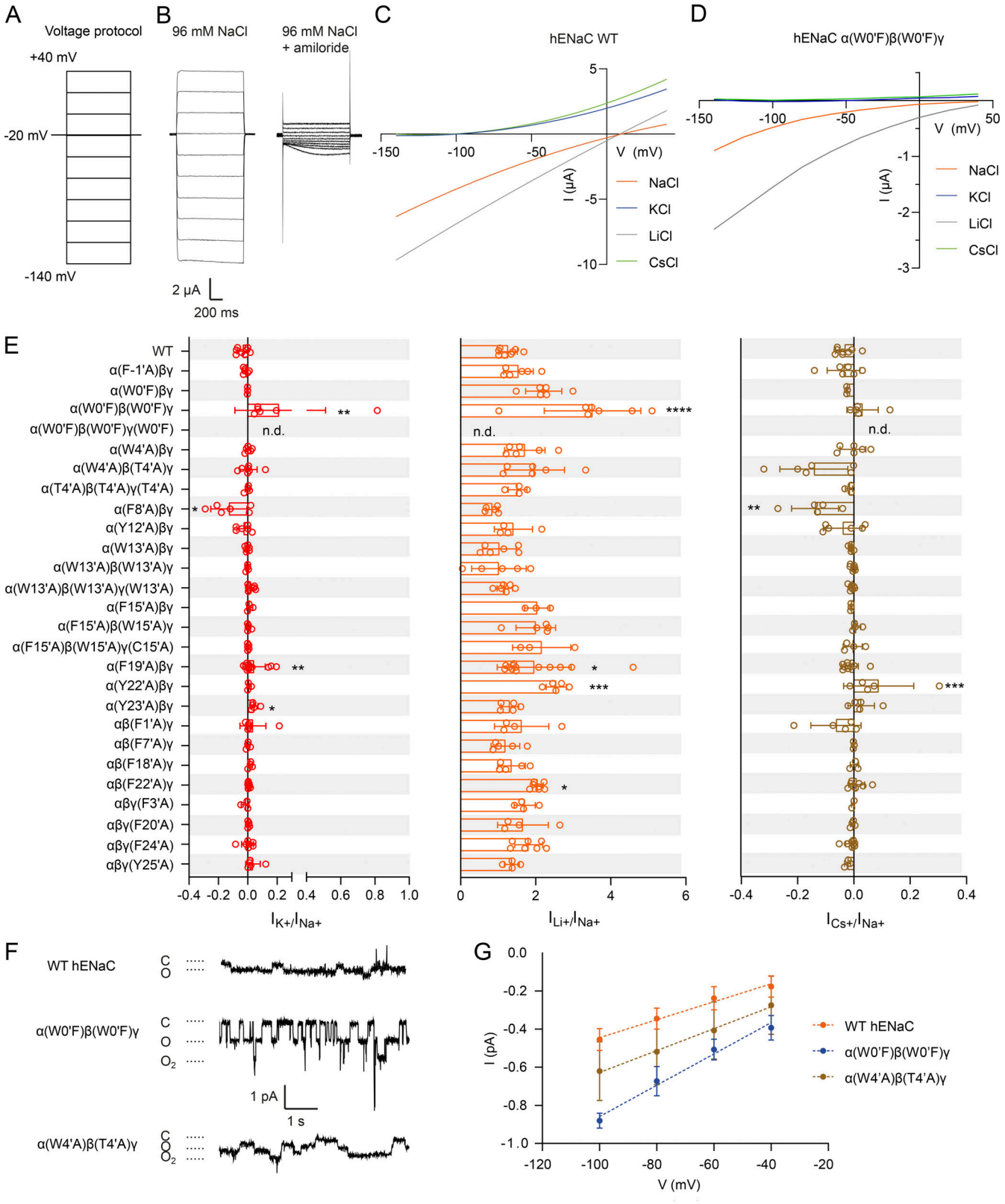

Figure 3. **M1 mutations in hENaC impact conductance but have only minimal effects on selectivity. (A)** Voltage protocol for relative amiloride-sensitive current measurements with different extracellular cations. *Xenopus* oocytes were injected with hENaC WT or mutant cRNA, and macroscopic currents were recording using two-electrode voltage clamping. *Xenopus* oocytes were clamped at −20 mV and continuously perfused with solution containing amiloride (100 µM), and currents were elicited upon switching the ECS to one without amiloride. After 1 min, the voltage protocol was applied. Currents were measured during 1-s voltage steps from a holding potential of −20 mV to test potentials of −140 mV to +40 mV in 20-mV increments. **(B and C)** Currents measured in the presence of 100 µM amiloride (C) were subtracted from currents measured in the absence of amiloride (B). **(C and D)** I-V relationships of the amiloride-

sensitive current in 96 mM Na^+, K^+, Li^+, and Cs^+ bath of WT hENaC and the designated mutant. **(E)** Relative $I_{K+/Na+}$ (red), I_{Li+}/I_{Na+} (orange), and I_{Cs+}/I_{Na+} (brown) current amplitudes measured at −100 mV in WT hENaC and the designated mutants. Values are shown as mean ± SD. Data were compared by one-way ANOVA with Dunnett's multiple comparisons test for comparison with control (WT hENaC). *, P < 0.05; **, P < 0.01; ***, P < 0.001; ****, P < 0.0001; n.d., not determined. **(F)** Single-channel traces of WT hENaC and designated mutants in the cell-attached configuration in *Xenopus* oocytes recorded at −100 mV. The spikes originate from endogenous mechanosensitive ion channels. **(G)** Single-channel I-V relationships for the channels shown in F. Slopes estimated by linear regression gave conductances as follows: WT = 4.7 ± 0.98 pS; α(W0′F)β(W0′F)γ = 8.6 ± 1.0 pS; (αW4′A; βT4′A)γ = 5.3 ± 2.2 pS. Data are presented as mean ± SD for four to seven patches. The value for α(W0′F)β(W0′F)γ is significantly greater than that of the WT channel (P = 0.0004).

that were equally permeable to Na^+, K^+, Li^+, and Cs^+. Additionally, the pH_{50} values of both mutants were drastically left-shifted to 7.3 ± 0.1 for H28A and 7.2 ± 0.0 for G29A, respectively. This is in agreement with previous work on the equivalent positions in ENaC (Kellenberger et al., 2002; Kucher et al., 2011). While alanine substitution at the conserved I33 resulted in a similar phenotype (loss of selectivity, left-shifted pH_{50}), mutation of K42 and R43 at the bottom of M1 showed a more modest reduction in Na^+ selectivity and a less pronounced effect on proton dependence: the K42Q mutant showed WT-like gating

Table 4. **Relative amiloride-sensitive currents in WT hENaC and hENaC M1 mutants**

Construct	I_K/I_{Na} (−100 mV)	I_{Li}/I_{Na} (−100 mV)	I_{Cs}/I_{Na} (−100 mV)	*n*
WT hENaC	−0.04 ± 0.04	1.2 ± 0.2	−0.04 ± 0.04	7
α(W-1′A)βγ	-0.02 ± 0.02	1.5 ± 0.4	−0.04 ± 0.06	6
α(W0′F)βγ	−0.02 ± 0.00	2.2 ± 0.5	−0.03 ± 0.00	6
α(W0′F)β(W0′F)γ	0.2 ± 0.3[a]	3.5 ± 1.3[b]	0.03 ± 0.06	5
α(W0′F)β(W0′F)γ(W0′F)	n.d.	n.d.	n.d.	
α(W4′A)βγ	0.00 ± 0.02	1.7 ± 0.5	0.0 ± 0.1	6
α(W4′A)β(T4′A)γ	0.00 ± 0.06	2.0 ± 0.9	−0.1 ± 0.1[c]	3–4
α(W4′A)β(T4′A)γ(T4′A)	0.00 ± 0.02	1.5 ± 0.3	−0.02 ± 0.01	4
α(F8′A)βγ	−0.1 ± 0.1[c]	0.9 ± 0.2	−0.1 ± 0.1[a]	5–6
α(Y12′A)βγ	−0.03 ± 0.05	1.4 ± 0.5	−0.04 ± 0.1	4–6
α(W13′A)βγ	−0.00 ± 0.01	1.0 ± 0.5	−0.01 ± 0.01	6
α(W13′A)β(W13′A)γ	−0.00 ± 0.01	1.0 ± 0.7	−0.00 ± 0.01	4–7
α(W13′A)β(W13′A)γ(W13′A)	0.02 ± 0.02	1.2 ± 0.2	−0.01 ± 0.01	6–8
α(F15′A)βγ	0.01 ± 0.02	2.0 ± 0.3	−0.01 ± 0.00	3
α(F15′A)β(W15′A)γ	0.01 ± 0.01	2.0 ± 0.5	0.01 ± 0.02	4–5
α(F15′A)β(W15′A)γ(C13′A)	0.00 ± 0.01	2.2 ± 0.8	−0.03 ± 0.01	3
α(F19′A)βγ	0.04 ± 0.08[a]	2.0 ± 1.0[c]	−0.01 ± 0.03	9–12
α(Y22′A)βγ	0.01 ± 0.01	2.6 ± 0.3[d]	0.09 ± 0.1[d]	3–5
α(Y23′A)βγ	0.05 ± 0.03[c]	1.3 ± 0.2	0.03 ± 0.05	5
αβ(F1′A)γ	0.0 ± 0.0	1.3 ± 0.2	−0.03 ± 0.04	3–4
αβ(F7′A)γ	0.0 ± 0.01	1.2 ± 0.4	−0.00 ± 0.00	3–5
αβ(F18′A)γ	0.02 ± 0.01	1.4 ± 0.4	0.00 ± 0.02	3–5
αβ(F22′A)γ	0.01 ± 0.01	2.1 ± 0.2[c]	0.01 ± 0.03	7–8
αβγ(F3′A)	−0.02 ± 0.03	1.7 ± 0.3	−0.00 ± 0.01	3–4
αβγ(F20′A)	0.01 ± 0.00	1.7 ± 0.7	−0.00 ± 0.01	4–5
αβγ(F24′A)	−0.0 ± 0.0	1.8 ± 0.47	−0.01 ± 0.02	7–8
αβγ(Y25′A)	0.04 ± 0.05	1.4 ± 0.20	−0.02 ± 0.01	3–5

Relative amiloride-sensitive currents determined for WT ENaC and hENaC mutants containing the designated amino acid substitutions at positions with aromatic side chain. Data are shown as mean ± SD; n.d., not determined. *n* refers to the number of individual oocytes. Values for mutants were compared with WT hENaC using one-way ANOVA with Dunnett's multiple comparisons test.
[a]P < 0.01.
[b]P < 0.0001.
[c]P < 0.05.
[d]P < 0.001.

Table 5. **Single-channel conductances of WT hENaC and 0′ and 4′ mutants**

Construct	Single-channel conductance (pS)	*n*
WT hENaC	4.7 ± 1.0	6
α(W0′F)βγ	7.4 ± 3.1[a]	5
α(W0′F)β(W0′F)γ	8.6 ± 1.0[b]	6
α(W4′A)βγ	6.6 ± 1.0	4
α(W4′A)β(T4′A)γ	5.3 ± 2.2	7

WT and mutant hENaC RNA was injected into *Xenopus* oocytes, and single-channel conductances were determined in the cell-attached patch-clamp configuration with 140 mM extracellular Na^+. Single-channel conductances are presented as mean ± SD and were compared with WT ENaC using one-way ANOVA with Dunnett's multiple comparisons test.
[a]$P < 0.05$.
[b]$P < 0.001$.

with slightly reduced ion selectivity (P_{Na+}/P_{K+} = 3.7 ± 0.3 and P_{Na+}/P_{Cs+} = 3.6 ± 1.7), while the R43Q mutant was slightly less sensitive to protons (pH_{50} 6.6 ± 0.1) and also displayed modestly reduced ion selectivity (P_{Na+}/P_{K+} = 6.8 ± 2.3 and P_{Na+}/P_{Cs+} = 15.0 ± 6.3). Interestingly, the mutants that exhibit large alkaline shifts in pH_{50} tend to also show distinct current phenotypes, where the peak current was typically followed by a sustained current (Fig. S7). Together, this complements the latest structural findings, which suggest that these residues contribute to the ion permeation pathway (Fig. S7), and mutational disruptions appear to cause severe consequences, manifested in abolished ion selectivity and altered gating.

In summary, our data on mASIC1a clearly show that the pre-M1 region is important for both ion selectivity and channel gating.

Determinants of ion selectivity in the pre-M1 of hENaC

Intrigued by the pronounced effects of mutations in the stretch of amino acids comprising the FASSST sequence motif in the pre-M1 region of mASIC1a, we sought to probe the potential role of the equivalent amino acids in the hENaC α, β, and γ subunits. To this end, alanine substitutions were introduced in one, two, or all three subunits of the FASSST sequence equivalent in hENaC. Additionally, two threonines immediately following this stretch of amino acids in the β and γ subunits of hENaC were mutated to valine (Fig. 5 A). None of the mutants were substantially different from WT hENaC in terms of the relative K^+/Na^+ and Cs^+/Na^+ current ratios, and Li^+/Na^+ current ratio was only modestly altered (Fig. 5 D). The only exception was the α(F62A)β(Y29A)γ double mutant, for which the Li^+/Na^+ current ratio was significantly increased from 1.2 ± 0.2 in WT to 3.7 ± 2.1 in α(F62A)β(Y29A)γ ($P < 0.0001$; Fig. 5 D and Table 7). The α(F62A)β(Y29A)γ(Y32A) and α(T66V)β(T33V)γ(T36V) triple mutants did not generate detectable currents.

Although these data suggest that the pre-M1 segment does not make a major contribution to ion selectivity in hENaC, we next tested if the amino acids corresponding to the mASIC1a FASSST sequence contribute to ion conduction. We thus determined single-channel conductances for (1) α(F62A)βγ and α(F62A)β(Y29A)γ (Table 8), because the equivalent aromatic amino acids at this position in mASIC1a play a role in ion selectivity and proton sensitivity (Fig. 4 C); and (2) mutants containing single T-to-V substitutions at all positions in this region containing the residue T (α(T66V)βγ, α(T66V)β(T33V)γ, α(T67V)βγ, αβ(T35V)γ, and αβγ(T38V); Fig. 5 A). Single-channel currents were not detectable for α(T67V)βγ, αβ(T35V)γ, and αβγ(T38V), but there was a marked increase in the single-channel conductance of the α(T66V)β(T33V)γ mutant compared with WT hENaC (Fig. 5, E and F; and Table 8). By contrast, the α(F62A)β(Y29A)γ double mutant showed only a small but insignificant increase in single-channel amplitude (Fig. 5, E and F; and Table 8).

Together, our data suggest that the pre-M1 region in hENaC is not a major determinant of ion selectivity but contributes to ion conduction.

Discussion

Recent advances in structural biology have resulted in the publication of multiple structures of cASIC1 and hENaC (Baconguis et al., 2014; Jasti et al., 2007; Noreng et al., 2018; Noreng et al., 2020; Yoder and Gouaux, 2020; Yoder et al., 2018). However, structures of open, full-length ASICs have not been obtained, and especially the conformation of the lower pore varies considerably among ASIC structures (Baconguis et al., 2014; Jasti et al., 2007; Yoder and Gouaux, 2020; Yoder et al., 2018). Similarly, the resolution of the pore-forming M1 and M2 segments in the available ENaC structures is comparatively low, giving rise to uncertainty regarding their absolute and relative positions, also with respect to the (unresolved) N- and C-termini (Noreng et al., 2018; Noreng et al., 2020). It is therefore difficult to reconcile the stark differences in ion selectivity among these channel types solely on the basis of available structural data. Here we use a combination of electrophysiological approaches to assess the contribution of M1 and pre-M1 to ion selectivity in mASIC1a and hENaC. We demonstrate that these regions contribute differently in both channel types: although mutations have severe consequences for ion selectivity in mASIC1a, they mostly affect conductance in hENaC. These findings support the notion that despite their similarities in sequence and structure, ASICs and ENaCs achieve ion selectivity via different mechanisms.

Both M1 and pre-M1 segments of mASIC1a contain key determinants of ion selectivity

In agreement with previous work, we found that mutations (Pfister et al., 2006; Poët et al., 2001) at the three native cysteines in ASIC1a M1 (C3′L, C13′W, and C15′F) do not have a major impact on ion selectivity or channel gating (Fig. 2 C). Similarly, other mutations along M1 between F23′ and G6′ do not change ion selectivity. By contrast, we found that mutations of aromatic side chains toward the intracellular end of M1 (F4′ and W0′) abolish sodium selectivity. We also observed significant changes in apparent proton sensitivity with W0′ mutants, which is consistent with earlier reports and supportive of the notion that this highly conserved side chain is important for channel gating

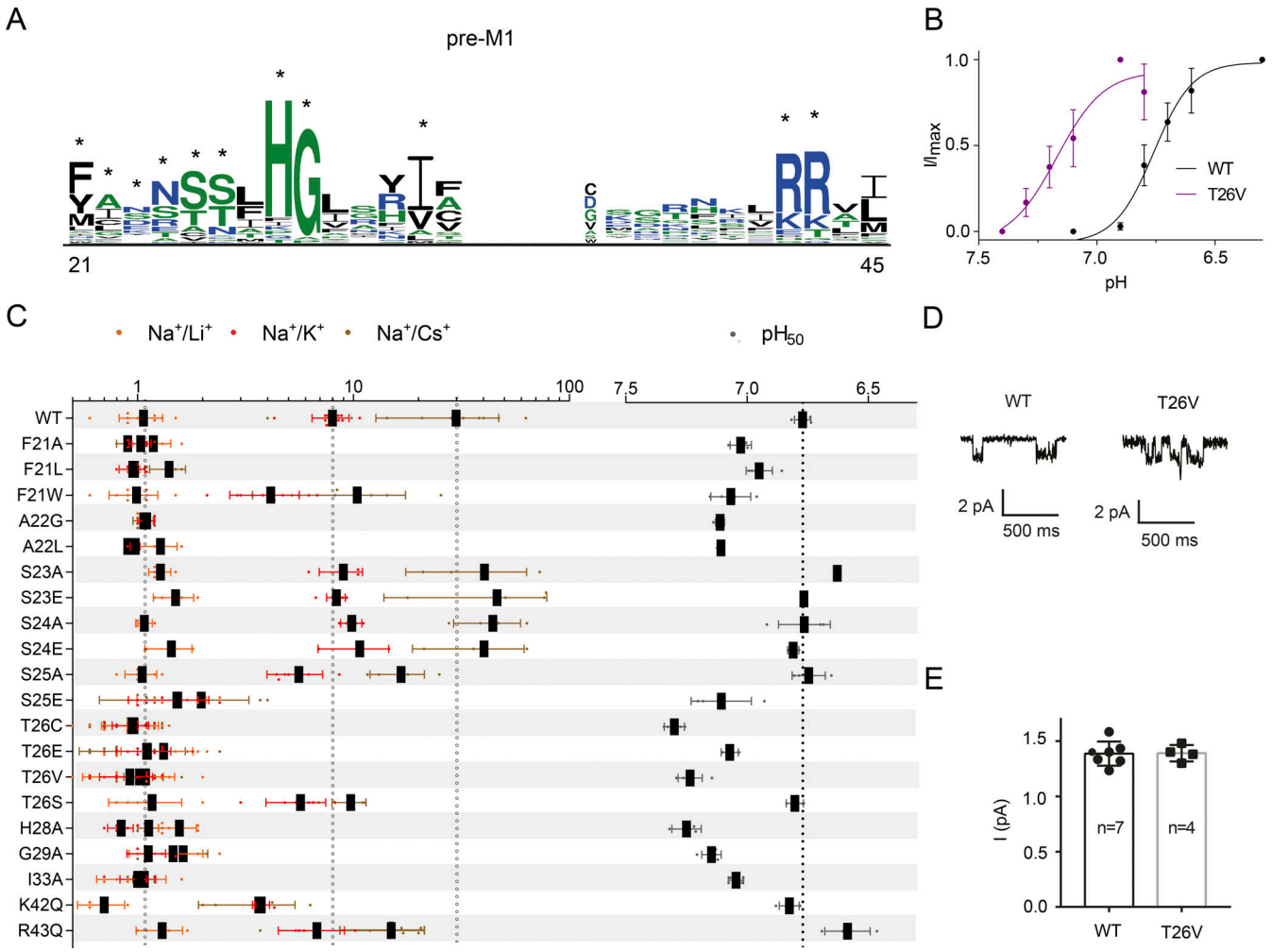

Figure 4. **Numerous mASIC1a pre-M1 mutations strongly impact ion selectivity and channel gating. (A)** Sequence logo based on 33 ASIC, ENaC, and related sequences (see Fig. S6). The height of each amino acid at a given position is proportional to its frequency at this position. The sequence logo was generated using the WebLogo 3 program (http://weblogo.threeplusone.com/create.cgi). The positions that were individually substituted in mASIC1a are highlighted with asterisks, and positions are numbered based on the position in mASIC1a. **(B)** pH concentration–response curves of WT mASIC1a and the T26V mutant. Data shown are mean ± SD; n = 5–6. **(C)** Residues that occur frequently in the DEG/ENaC superfamily of ion channels were mutated in mASIC1a to the indicated amino acids to assess their contributions to ion selectivity and proton sensitivity. Relative ion permeability ratios (shown on a logarithmic scale for clarity) and effective proton concentration pH_{50} values of mASIC1a WT and pre-M1 mutants. Values are presented as mean ± SD; $n \geq 4$. **(D)** Single-channel traces recorded in *Xenopus* oocytes expressing WT mASIC1a and the T26V mutant determined in outside-out patches. Cells were clamped at −60 mV and continuously perfused with pH 8.0 solution (in mM: 140 NaCl, 3 $MgCl_2$, and 5 HEPES) and activated with pH 6. The ICS contained (in mM): 110 NMDG, 2 $MgCl_2$, 2 $CaCl_2$, 10 HEPES, and 5 EGTA, pH 7.3. **(E)** Averaged single-channel current at −60 mV. Data are shown as individual data points with mean ± SD.

(Kasimova et al., 2020; Li et al., 2011). F4′ mutants, however, had WT-like gating and only affected ion selectivity. We therefore considered the F4′A mutant a reasonable model to test the notion that reduced bulk in the lower M1 may lower ion selectivity by increasing pore diameter. The finding that larger cations, such as MA^+, EMA^+, and EA^+, permeate F4′A mutant channels more readily than WT channels lends direct support to this hypothesis. We conclude that the two aromatic residues in lower M1, W0′ and F4′ indirectly contribute to the pore diameter and likely the overall structure of the mASIC1a lower pore.

Additionally, these results pointed toward the lower pore as a major determinant for ion selectivity in ASICs. Although the exact location of the selectivity filter in ASICs has remained a matter of debate, these findings support the notion that the selectivity filter might be located in the lower pore (Lynagh et al., 2020; Lynagh et al., 2017). This led us to postulate that M2-E18′ and M2-D21′ are likely to form the selectivity filter in ASICs. However, the recent cASIC1 structures clearly show that, at least in closed and desensitized conformations, it is the pre-M1 region that lines the lower ion permeation pathway, thus calling into question whether M2-E18′ and M2-D21′ make direct contributions to ion selectivity in the open state of ASICs (Yoder and Gouaux, 2020). The structures raise the possibility that the ASIC selectivity filter might be formed, at least in part, by the pre-M1 segment, specifically the narrow constriction formed at the histidine from the conserved HG motif that is involved in a network of both intra- and intersubunit interactions (Yoder and Gouaux, 2020). This is in agreement with our finding that the

Table 6. **Relative ion permeabilities and pH_{50} values of mASIC1a mutants**

Construct	P_{Na+}/P_{K+}	P_{Na+}/P_{Li+}	P_{Cs+}/P_{Na+}	pH_{50}
WT	8.0 ± 1.6	1.1 ± 0.2	29.9 ± 17.2	6.8 ± 0.03
F21A	1.0 ± 0.1[a]	1.2 ± 0.2	0.9 ± 0.1[b]	7.0 ± 0.04[a]
F21L	1.0 ± 0.1[a]	1.0 ± 0.1	1.4 ± 0.3[b]	7.1 ± 0.05[c]
F21W	4.1 ± 1.5[a]	1.0 ± 0.3	10.4 ± 7.0[b]	7.1 ± 0.08[a]
A22G	1.1 ± 0.1[a]	1.1 ± 0.1	1.1 ± 0.1[b]	7.1 ± 0.02[a]
A22L	1.0 ± 0.1[a]	1.3 ± 0.3	0.9 ± 0.0[c]	7.1 ± 0.01[a]
S23A	9.0 ± 2.0	1.3 ± 0.2	40.4 ± 22.9	6.6 ± 0.01
S23E	8.3 ± 0.8	1.5 ± 0.3	46.2 ± 32.4	6.8 ± 0.01
S24A	9.8 ± 1.1	1.1 ± 0.1	44.2 ± 15.1	6.8 ± 0.1
S24E	10.7 ± 3.9[b]	n.d.	40.3 ± 21.5	6.8 ± 0.02
S25A	5.6 ± 1.6[b]	1.1 ± 0.2	16.6 ± 4.7	6.8 ± 0.07
S25E	1.5 ± 0.6[a]	1.5 ± 0.5	2.0 ± 1.3[a]	7.1 ± 0.1[a]
T26C	0.9 ± 0.2[a]	1.0 ± 0.3	1.0 ± 0.2[a]	7.1 ± 0.03[a]
T26E	1.1 ± 0.3[a]	1.3 ± 0.5	1.1 ± 0.6[a]	7.2 ± 0.05[a]
T26V	0.9 ± 0.3[a]	1.0 ± 0.5	1.1 ± 0.2[a]	7.2 ± 0.04[a]
T26S	5.7 ± 1.8[b]	1.2 ± 0.4	9.7 ± 1.7[d]	6.8 ± 0.04
H28A	0.8 ± 0.1[a]	1.6 ± 0.3	1.1 ± 0.1[c]	7.3 ± 0.06[a]
G29A	1.1 ± 0.2[a]	1.5 ± 0.6	1.6 ± 0.5 [c]	7.2 ± 0.04[a]
I33A	1.0 ± 0.2[a]	1.0 ± 0.4	1.1 ± 0.1 [c]	7.0 ± 0.03[a]
K42Q	3.7 ± 0.3[a]	0.7 ± 0.2	3.6 ± 1.7 [c]	6.8 ± 0.04
R43Q	6.8 ± 2.3	1.3 ± 0.3	15.0 ± 6.3	6.6 ± 0.09[c]

Relative ion permeabilities and pH_{50} values of WT mASIC1a and mutants containing amino acid substitutions in the pre-M1 region. Data are shown as mean ± SD with $n \geq 4$, where n refers to the number of individual oocytes; n.d., not determined. Values for mutants were compared with WT using one-way ANOVA with Dunnett's multiple comparisons test.
[a]$P < 0.0001$.
[b]$P < 0.01$.
[c]$P < 0.001$.
[d]$P < 0.05$.

pre-M1 segment of mASIC1a is extremely sensitive to mutations, such that even minor mutational disruptions abolish ion selectivity, including those to the HG motif (Fig. 4 C). In fact, this protein segment contains numerous side chains that, when mutated, have drastic consequences for both ion selectivity and channel gating, therefore underlining its functional importance. By comparison, we found relatively fewer side chains in the pore-lining M2 segment to affect ion selectivity (Lynagh et al., 2020; Lynagh et al., 2017).

Together, these data are in agreement with the possibility that the selectivity filter is located at the lower end of the pore, likely formed by the pre-M1 segment and at least indirectly supported by E18′ and D21′ in M2 and W0′ and F4′ in M1. However, in the absence of an open channel structure with a fully resolved pre-M1 region, we cannot rule out the possibility that other side chains, including M2-E18′ and M2-D21′, may directly line the permeation pathway in the channel open state. Interestingly, none of the mutations tested in this study increases the ion selectivity of ASIC1a. Because ENaC is more Na^+ selective than ASIC, but none of the numerous ASIC mutations, even to ENaC-like identity, markedly increase Na^+ selectively, ASICs seem to have developed, independently of ENaCs, a fragility in their molecular blueprint for ion selectivity.

ENaC ion selectivity is comparatively impervious to mutations in M1 and pre-M1

Although structural information on the ENaC pore is of relatively low resolution (Noreng et al., 2018; Noreng et al., 2020), there is strong functional evidence that the G/SXS motif in the middle of the pore is critical for ion selectivity in ENaCs (Kellenberger et al., 2001; Kellenberger et al., 2002; Kellenberger et al., 1999b; Yang and Palmer, 2018). Additionally, and in contrast to the findings for ASICs, the negatively charged side chains in the M2-18′ and M2-21′ positions do not appear to play a crucial role in ion selectivity (Yang and Palmer, 2018). Yet, it is interesting to note that mutations to W0′ in the ENaC α and β subunits affected both selectivity and single-channel conductance. Although the triple mutant was nonfunctional, this points toward W0′ being—directly or indirectly—involved in ion conduction in ENaCs (Fig. 2), although likely to a lesser degree than in ASICs. Furthermore, important functional contributions by side chains in the (putative) lower pore of ENaCs are highlighted by the findings that mutations to the conserved HG motif affect gating by decreasing ENaC open probability (Kellenberger et al., 2002) and that mutations of the G in this motif cause pseudohypoaldosteronism type 1 in humans (Kucher et al., 2011). Our results expand on these results by showing that selected pre-M1 mutations can affect ion selectivity or conductance (Fig. 5). This shows that, in contrast to ASICs, mutations at a few positions in both the middle and lower parts of the pore have relatively minor effects on ion selectivity but contribute significantly to conduction in ENaCs. Additionally, reducing the bulk of aromatic side chains along the entire length of at least the α subunit M1 in hENaC, such as W0′, F8′, F19′, Y22′, and Y23′, can lead to (albeit small) changes in ion selectivity.

This indicates that although the overall ion selectivity profile is maintained in most ENaC mutants, subtle changes can be elicited by mutations throughout the M1 and pre-M1 segments. By contrast, mutations in the upper and middle sections of both M1 and M2 of ASICs do not result in changed ion selectivity (the only exception being C15′F; see Fig. 2 C). We thus conclude that the open pore structures of ASICs and ENaCs likely display important structural differences.

Limitations and outlook

In the majority of our work on ASICs, we rely on relative ion permeability ratios as a proxy for ion selectivity. More subtle changes in conductance, as revealed for selected ENaC mutants, are therefore harder to assess in measurements of relative ion permeability ratios. But previous studies demonstrate that relative ion permeability measurements can result in robust estimates of ion selectivity (Kellenberger et al., 2001; Kellenberger et al., 1999a; Lynagh et al., 2020; Lynagh et al., 2017). Also, and in line with work by others (Yang and Palmer, 2018), some of the ENaC triple mutants did not generate measurable currents. We

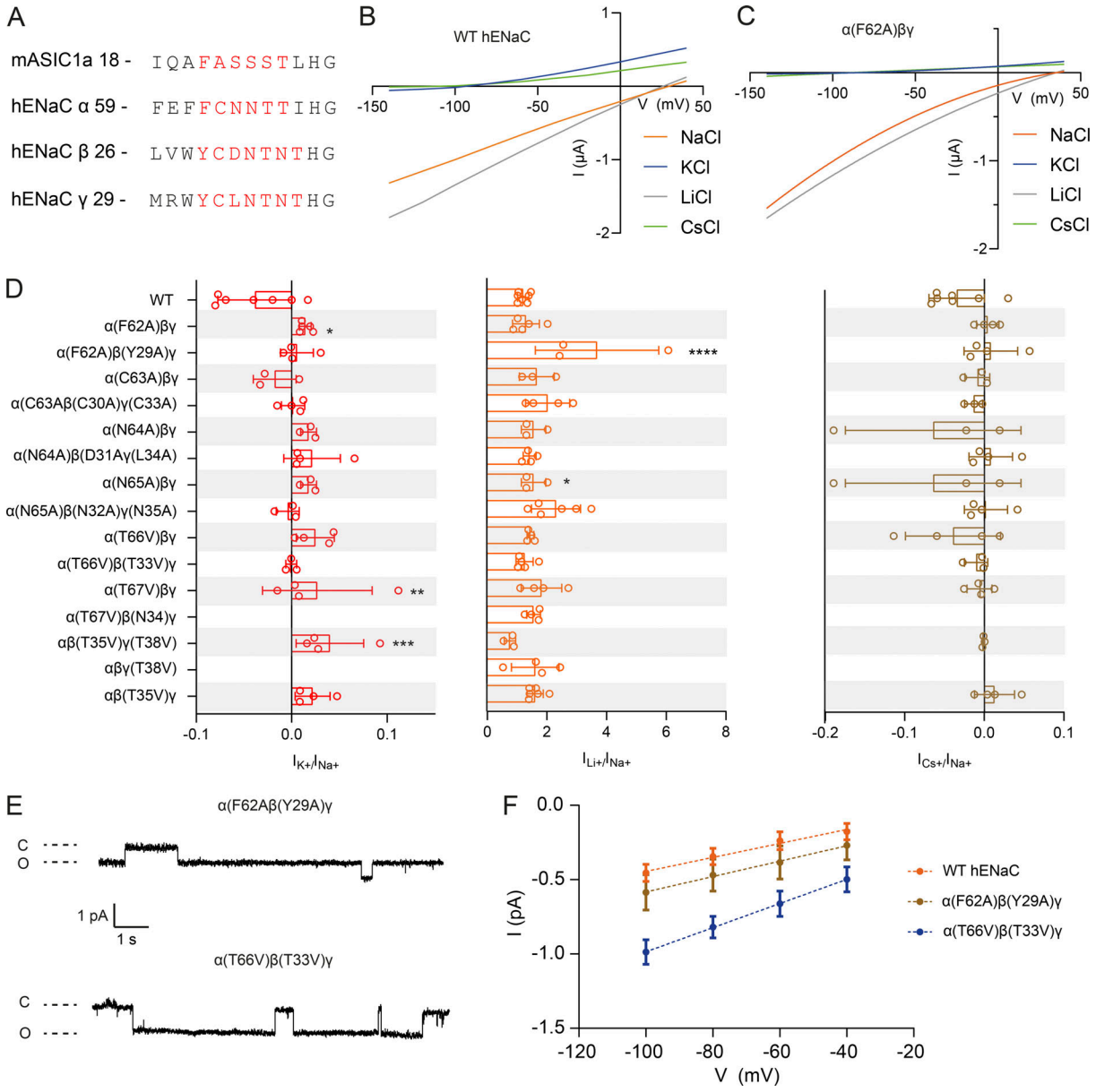

Figure 5. **Pre-M1 mutations in hENaC primarily alter conductance but not ion selectivity. (A)** Sequence alignment of part of the pre-M1 region of mASIC1a and hENaC. Residues that were mutated individually are highlighted in red. **(B and C)** I-V relationships of the amiloride-sensitive currents for WT hENaC (B) and the designated mutant (C). **(D)** Relative amiloride-sensitive I_{K+}/I_{Na+} (red), I_{Li+}/I_{Na+} (orange), and I_{Cs+}/I_{Na+} (brown) currents measured at −100 mV in WT hENaC and the designated mutants. Values are shown as mean ± SD. Data were compared by one-way ANOVA with Dunnett's multiple comparisons test for comparison with control (WT hENaC). *, P < 0.05; **, P < 0.01; ***, P < 0.001; ****, P < 0.0001. **(E)** Single-channel currents of depicted hENaC mutants. Currents were recorded in *Xenopus* oocytes expressing hENaC channels using the cell-attached patch-clamp configuration at a holding potential of +100 mV with 140 mM NaCl in the pipette. **(F)** Single-channel I-V relationships for the channels shown in C. Data are presented as mean ± SD. Slopes estimated by linear regression resulted in the following conductances: WT = 4.7 ± 1.0 pS; α(T66V)β(T33V) = 8.6 ± 1.0 pS; α(F62A)β(Y29A)γ = 5.2 ± 0.3 pS. Data are presented as mean ± SD for four to seven patches. The value for α(T66V)β(T33V)γ is significantly greater than that of the WT channel (P = 0.0004).

therefore cannot exclude the possibility that we may have underestimated the contributions of some side chains to selectivity and/or conductance. Additionally, it has been reported that the ENaC pore helices might be arranged asymmetrically and that mutations at equivalent sites may not cause equivalent effects (Li et al., 2003). Finally, the lack of definitive structural information on the open pore structures of both ASICs and ENaCs means that it is difficult to interpret our functional data in a detailed structural context.

Overall, however, the data at hand clearly support the notion of ASICs and ENaCs achieving sodium selectivity by different mechanisms. Our work therefore highlights how related channels can achieve different functional properties despite obvious sequence conservation in, for example, the (at least partially) pore-lining M2 segments. Instead, the data indicate that the non–pore-lining M1 segment indirectly contributes to ion selectivity in both ASICs and ENaCs.

Table 7. **Relative amiloride-sensitive currents in WT hENaC and hENaC mutants**

Construct	I_K/I_{Na} (−100mV)	I_{Li}/I_{Na} (−100mV)	I_{Cs}/I_{Na} (−100 mV)
WT hENaC	−0.04 ± 0.04	1.2 ± 0.2	−0.04 ± 0.04
αβ(T35V)γ	0.02 ± 0.02[a]	1.6 ± 0.3	0.01 ± 0.03
αβγ(T38V)	n.d.	1.6 ± 0.8	n.d.
αβ(T35V)γ(T38V)	0.04 ± 0.04[b]	0.8 ± 0.2	−0.00 ± 0.00
α(T67V)β(N34A)γ	n.d.	1.6 ± 0.2	n.d.
α(T67V)βγ	0.03 ± 0.06[c]	1.8 ± 0.7	−0.01 ± 0.02
α(T66V)β(T33V) γ	−0.00 ± 0.01	1.3 ± 0.3	−0.01 ± 0.02
α(T66V)βγ	0.03 ± 0.02[c]	1.5 ± 0.1	−0.04 ± 0.06
α(N65A)β(N32A)γ(N35A)	−0.00 ± 0.01	2.3 ± 0.8[a]	0.00 ± 0.03
α(N65A)βγ	0.02 ± 0.01	1.6 ± 0.4	−0.06 ± 0.11
α(N64A)β(D31A)γ(L34A)	0.02 ± 0.03[a]	1.4 ± 0.2	0.01 ± 0.03
α(N64A)βγ	0.02 ± 0.01	1.6 ± 0.4	−0.06 ± 0.11
α(C63A)β(C30A)γ(C33A)	0.00 ± 0.01	2.0 ± 0.7	−0.01 ± 0.01
α(C63A)βγ	−0.02 ± 0.02	1.7 ± 0.6	−0.01 ± 0.02
α(F62A)β(Y29A)γ	0.01 ± 0.02	3.7 ± 2.1[d]	0.01 ± 0.03
α(F62A)βγ	0.01 ± 0.01[a]	1.3 ± 0.5	0.00 ± 0.01

Relative amiloride-sensitive currents determined for WT hENaC and hENaC mutants containing the designated amino acid substitutions. Data are shown as mean ± SD, and *n* refers to the number of individual oocytes; n.d., not determined. Values for mutants were compared with WT hENaC using one-way ANOVA with Dunnett's multiple comparisons test; *n* = 3–7.
[a]P < 0.05.
[b]P < 0.001.
[c]P < 0.01.
[d]P < 0.0001.

Table 8. **Single-channel conductances of WT hENaC and pre-M1 mutants**

Construct	Single channel conductance (pS)	*n*
WT hENaC	4.7 ± 1.0	6
α(F62A)βγ	4.5 ± 1.0	5
α(F62A)β(Y29A)γ	5.2 ± 0.3	5
α(T66V)βγ	7.1 ± 0.6[a]	7
α(T66V)β(T33V)γ	8.1 ± 0.6[b]	5

WT and mutant hENaC RNA was injected into *Xenopus* oocytes, and single-channel conductances were determined in the cell-attached patch-clamp configuration with 140 mM extracellular Na^+. Single-channel conductances are presented as mean ± SD and were compared with WT ENaC using one-way ANOVA with Dunnett's multiple comparisons test.
[a]P < 0.05.
[b]P < 0.05.

Acknowledgments

Christopher J. Lingle served as editor.

This work was supported by Lundbeckfonden (R171-2014-558, to T. Lynagh; R139-2012-12390, to S.A. Pless), the Danmarks Frie Forskningsfond (4092-00348B, to T. Lynagh), and Carlsbergfondet (2013_01_0439, to S.A. Pless).

S. Friis is a full-time employee of Nanion Technologies. The other authors declare no competing financial interests.

Author contributions: Z.P. Sheikh, T. Lynagh, M. Wulf, and S. Friis conducted functional experiments; Z.P. Sheikh, T. Lynagh, M. Wulf, S. Friis, and M. Althaus analyzed data; Z.P. Sheikh, T. Lynagh, M. Althaus, and S.A. Pless conceptualized the work; Z.P. Sheikh and S.A. Pless drafted the manuscript and finalized it with input from all authors.

Submitted: 16 February 2021
Accepted: 26 July 2021

References

Arnadóttir, J., R. O'Hagan, Y. Chen, M.B. Goodman, and M. Chalfie. 2011. The DEG/ENaC protein MEC-10 regulates the transduction channel complex in *Caenorhabditis elegans* touch receptor neurons. *J. Neurosci.* 31: 12695–12704. https://doi.org/10.1523/JNEUROSCI.4580-10.2011

Baconguis, I., C.J. Bohlen, A. Goehring, D. Julius, and E. Gouaux. 2014. X-ray structure of acid-sensing ion channel 1-snake toxin complex reveals open state of a Na^+-selective channel. *Cell.* 156:717–729. https://doi.org/10.1016/j.cell.2014.01.011

Borg, C.B., N. Braun, S.A. Heusser, Y. Bay, D. Weis, I. Galleano, C. Lund, W. Tian, L.M. Haugaard-Kedström, E.P. Bennett, et al. 2020. Mechanism and site of action of big dynorphin on ASIC1a. *Proc. Natl. Acad. Sci. USA.* 117:7447–7454. https://doi.org/10.1073/pnas.1919323117

Braun, N., S.Friis, C. Ihling, A. Sinz, J. Andersen, and S.A. Pless. 2021. High-throughput characterization of photocrosslinker-bearing ion channel variants to map residues critical for function and pharmacology. *bioRxiv.* doi: (Preprint posted May 7, 2021)https://doi.org/10.1101/2020.11.24.392498

Chen, C.C., A. Zimmer, W.H. Sun, J. Hall, M.J. Brownstein, and A. Zimmer. 2002. A role for ASIC3 in the modulation of high-intensity pain stimuli.

Proc. Natl. Acad. Sci. USA. 99:8992–8997. https://doi.org/10.1073/pnas.122245999

Cheng, Y.R., B.Y. Jiang, and C.C. Chen. 2018. Acid-sensing ion channels: dual function proteins for chemo-sensing and mechano-sensing. *J. Biomed. Sci.* 25:46. https://doi.org/10.1186/s12929-018-0448-y

Coscoy, S., J.R. de Weille, E. Lingueglia, and M. Lazdunski. 1999. The pre-transmembrane 1 domain of acid-sensing ion channels participates in the ion pore. *J. Biol. Chem.* 274:10129–10132. https://doi.org/10.1074/jbc.274.15.10129

Dahan, D.S., M.I. Dibas, E.J. Petersson, V.C. Auyeung, B. Chanda, F. Bezanilla, D.A. Dougherty, and H.A. Lester. 2004. A fluorophore attached to nicotinic acetylcholine receptor β M2 detects productive binding of agonist to the α δ site. *Proc. Natl. Acad. Sci. USA.* 101:10195–10200. https://doi.org/10.1073/pnas.0301885101

Dougherty, D.A., and E.B. Van Arnam. 2014. In vivo incorporation of non-canonical amino acids by using the chemical aminoacylation strategy: a broadly applicable mechanistic tool. *ChemBioChem.* 15:1710–1720. https://doi.org/10.1002/cbic.201402080

Duan, B., L.J. Wu, Y.Q. Yu, Y. Ding, L. Jing, L. Xu, J. Chen, and T.L. Xu. 2007. Upregulation of acid-sensing ion channel ASIC1a in spinal dorsal horn neurons contributes to inflammatory pain hypersensitivity. *J. Neurosci.* 27:11139–11148. https://doi.org/10.1523/JNEUROSCI.3364-07.2007

Duan, B., D.S. Liu, Y. Huang, W.Z. Zeng, X. Wang, H. Yu, M.X. Zhu, Z.Y. Chen, and T.L. Xu. 2012. PI3-kinase/Akt pathway-regulated membrane insertion of acid-sensing ion channel 1a underlies BDNF-induced pain hypersensitivity. *J. Neurosci.* 32:6351–6363. https://doi.org/10.1523/JNEUROSCI.4479-11.2012

Gründer, S., N.F. Jaeger, I. Gautschi, L. Schild, and B.C. Rossier. 1999. Identification of a highly conserved sequence at the N-terminus of the epithelial Na^+ channel alpha subunit involved in gating. *Pflugers Arch.* 438:709–715. https://doi.org/10.1007/s004249900119

Haerteis, S., B. Krueger, C. Korbmacher, and R. Rauh. 2009. The delta-subunit of the epithelial sodium channel (ENaC) enhances channel activity and alters proteolytic ENaC activation. *J. Biol. Chem.* 284:29024–29040. https://doi.org/10.1074/jbc.M109.018945

Hanukoglu, I., and A. Hanukoglu. 2016. Epithelial sodium channel (ENaC) family: Phylogeny, structure-function, tissue distribution, and associated inherited diseases. *Gene.* 579:95–132. https://doi.org/10.1016/j.gene.2015.12.061

Jasti, J., H. Furukawa, E.B. Gonzales, and E. Gouaux. 2007. Structure of acid-sensing ion channel 1 at 1.9 A resolution and low pH. *Nature.* 449:316–323. https://doi.org/10.1038/nature06163

Kashlan, O.B., and T.R. Kleyman. 2011. ENaC structure and function in the wake of a resolved structure of a family member. *Am. J. Physiol. Renal Physiol.* 301:F684–F696. https://doi.org/10.1152/ajprenal.00259.2011

Kasimova, M.A., T. Lynagh, Z.P. Sheikh, D. Granata, C.B. Borg, V. Carnevale, and S.A. Pless. 2020. Evolutionarily conserved interactions within the pore domain of acid-sensing ion channels. *Biophys. J.* 118:861–872. https://doi.org/10.1016/j.bpj.2019.09.001

Kellenberger, S., I. Gautschi, and L. Schild. 1999a. A single point mutation in the pore region of the epithelial Na^+ channel changes ion selectivity by modifying molecular sieving. *Proc. Natl. Acad. Sci. USA.* 96:4170–4175. https://doi.org/10.1073/pnas.96.7.4170

Kellenberger, S., N. Hoffmann-Pochon, I. Gautschi, E. Schneeberger, and L. Schild. 1999b. On the molecular basis of ion permeation in the epithelial Na^+ channel. *J. Gen. Physiol.* 114:13–30. https://doi.org/10.1085/jgp.114.1.13

Kellenberger, S., M. Auberson, I. Gautschi, E. Schneeberger, and L. Schild. 2001. Permeability properties of ENaC selectivity filter mutants. *J. Gen. Physiol.* 118:679–692. https://doi.org/10.1085/jgp.118.6.679

Kellenberger, S., I. Gautschi, and L. Schild. 2002. An external site controls closing of the epithelial Na^+ channel ENaC. *J. Physiol.* 543:413–424. https://doi.org/10.1113/jphysiol.2002.022020

Kellenberger, S., I. Gautschi, Y. Pfister, and L. Schild. 2005. Intracellular thiol-mediated modulation of epithelial sodium channel activity. *J. Biol. Chem.* 280:7739–7747. https://doi.org/10.1074/jbc.M409955200

Kucher, V., N. Boiko, O. Pochynyuk, and J.D. Stockand. 2011. Voltage-dependent gating underlies loss of ENaC function in Pseudohypoaldosteronism type 1. *Biophys. J.* 100:1930–1939. https://doi.org/10.1016/j.bpj.2011.02.046

Li, J., S. Sheng, C.J. Perry, and T.R. Kleyman. 2003. Asymmetric organization of the pore region of the epithelial sodium channel. *J. Biol. Chem.* 278:13867–13874. https://doi.org/10.1074/jbc.M300149200

Li, T., Y. Yang, and C.M. Canessa. 2011. Outlines of the pore in open and closed conformations describe the gating mechanism of ASIC1. *Nat. Commun.* 2:399. https://doi.org/10.1038/ncomms1409

Lingueglia, E., J.R. de Weille, F. Bassilana, C. Heurteaux, H. Sakai, R. Waldmann, and M. Lazdunski. 1997. A modulatory subunit of acid sensing ion channels in brain and dorsal root ganglion cells. *J. Biol. Chem.* 272:29778–29783. https://doi.org/10.1074/jbc.272.47.29778

Lynagh, T., E. Flood, C. Boiteux, M. Wulf, V.V. Komnatnyy, J.M. Colding, T.W. Allen, and S.A. Pless. 2017. A selectivity filter at the intracellular end of the acid-sensing ion channel pore. *eLife.* 6:e24630. https://doi.org/10.7554/eLife.24630

Lynagh, T., E. Flood, C. Boiteux, Z.P. Sheikh, T.W. Allen, and S.A. Pless. 2020. Determinants of ion selectivity in ASIC1a- and ASIC2a-containing acid-sensing ion channels. *J. Gen. Physiol.* 152:e201812297. https://doi.org/10.1085/jgp.201812297

Mazzuca, M., C. Heurteaux, A. Alloui, S. Diochot, A. Baron, N. Voilley, N. Blondeau, P. Escoubas, A. Gélot, A. Cupo, et al. 2007. A tarantula peptide against pain via ASIC1a channels and opioid mechanisms. *Nat. Neurosci.* 10:943–945. https://doi.org/10.1038/nn1940

Noreng, S., A. Bharadwaj, R. Posert, C. Yoshioka, and I. Baconguis. 2018. Structure of the human epithelial sodium channel by cryo-electron microscopy. *eLife.* 7:e39340. https://doi.org/10.7554/eLife.39340

Noreng, S., R. Posert, A. Bharadwaj, A. Houser, and I. Baconguis. 2020. Molecular principles of assembly, activation, and inhibition in epithelial sodium channel. *eLife.* 9:e59038. https://doi.org/10.7554/eLife.59038

Palmer, L.G. 1982. Ion selectivity of the apical membrane Na channel in the toad urinary bladder. *J. Membr. Biol.* 67:91–98. https://doi.org/10.1007/BF01868651

Palmer, L.G. 1985. Interactions of amiloride and other blocking cations with the apical Na channel in the toad urinary bladder. *J. Membr. Biol.* 87:191–199. https://doi.org/10.1007/BF01871218

Palmer, L.G. 1990. Epithelial Na channels: the nature of the conducting pore. *Ren. Physiol. Biochem.* 13:51–58. https://doi.org/10.1159/000173347

Pfister, Y., I. Gautschi, A.N. Takeda, M. van Bemmelen, S. Kellenberger, and L. Schild. 2006. A gating mutation in the internal pore of ASIC1a. *J. Biol. Chem.* 281:11787–11791. https://doi.org/10.1074/jbc.M513692200

Poët, M., M. Tauc, E. Lingueglia, P. Cance, P. Poujeol, M. Lazdunski, and L. Counillon. 2001. Exploration of the pore structure of a peptide-gated Na^+ channel. *EMBO J.* 20:5595–5602. https://doi.org/10.1093/emboj/20.20.5595

Rossier, B.C., M.E. Baker, and R.A. Studer. 2015. Epithelial sodium transport and its control by aldosterone: the story of our internal environment revisited. *Physiol. Rev.* 95:297–340. https://doi.org/10.1152/physrev.00011.2014

Schild, L., E. Schneeberger, I. Gautschi, and D. Firsov. 1997. Identification of amino acid residues in the alpha, beta, and gamma subunits of the epithelial sodium channel (ENaC) involved in amiloride block and ion permeation. *J. Gen. Physiol.* 109:15–26. https://doi.org/10.1085/jgp.109.1.15

Wang, Y.Z., J.J. Wang, Y. Huang, F. Liu, W.Z. Zeng, Y. Li, Z.G. Xiong, M.X. Zhu, and T.L. Xu. 2015. Tissue acidosis induces neuronal necroptosis via ASIC1a channel independent of its ionic conduction. *eLife.* 4:e05682. https://doi.org/10.7554/eLife.05682

Wemmie, J.A., J. Chen, C.C. Askwith, A.M. Hruska-Hageman, M.P. Price, B.C. Nolan, P.G. Yoder, E. Lamani, T. Hoshi, J.H. Freeman Jr., and M.J. Welsh. 2002. The acid-activated ion channel ASIC contributes to synaptic plasticity, learning, and memory. *Neuron.* 34:463–477. https://doi.org/10.1016/S0896-6273(02)00661-X

Wichmann, L., J.S. Dulai, J. Marles-Wright, S. Maxeiner, P.P. Szczesniak, I. Manzini, and M. Althaus. 2019. An extracellular acidic cleft confers profound H^+-sensitivity to epithelial sodium channels containing the δ-subunit in *Xenopus laevis*. *J. Biol. Chem.* 294:12507–12520. https://doi.org/10.1074/jbc.RA119.008255

Xiong, Z.G., and T.L. Xu. 2012. The role of ASICS in cerebral ischemia. *Wiley Interdiscip. Rev. Membr. Transp. Signal.* 1:655–662. https://doi.org/10.1002/wmts.57

Yang, L., and L.G. Palmer. 2018. Determinants of selective ion permeation in the epithelial Na^+ channel. *J. Gen. Physiol.* 150:1397–1407. https://doi.org/10.1085/jgp.201812164

Yoder, N., and E. Gouaux. 2020. The His-Gly motif of acid-sensing ion channels resides in a reentrant 'loop' implicated in gating and ion selectivity. *eLife.* 9:e56527. https://doi.org/10.7554/eLife.56527

Yoder, N., C. Yoshioka, and E. Gouaux. 2018. Gating mechanisms of acid-sensing ion channels. *Nature.* 555:397–401. https://doi.org/10.1038/nature25782

Ziemann, A.E., J.E. Allen, N.S. Dahdaleh, I.I. Drebot, M.W. Coryell, A.M. Wunsch, C.M. Lynch, F.M. Faraci, M.A. Howard III, M.J. Welsh, and J.A. Wemmie. 2009. The amygdala is a chemosensor that detects carbon dioxide and acidosis to elicit fear behavior. *Cell.* 139:1012–1021. https://doi.org/10.1016/j.cell.2009.10.029

Supplemental material

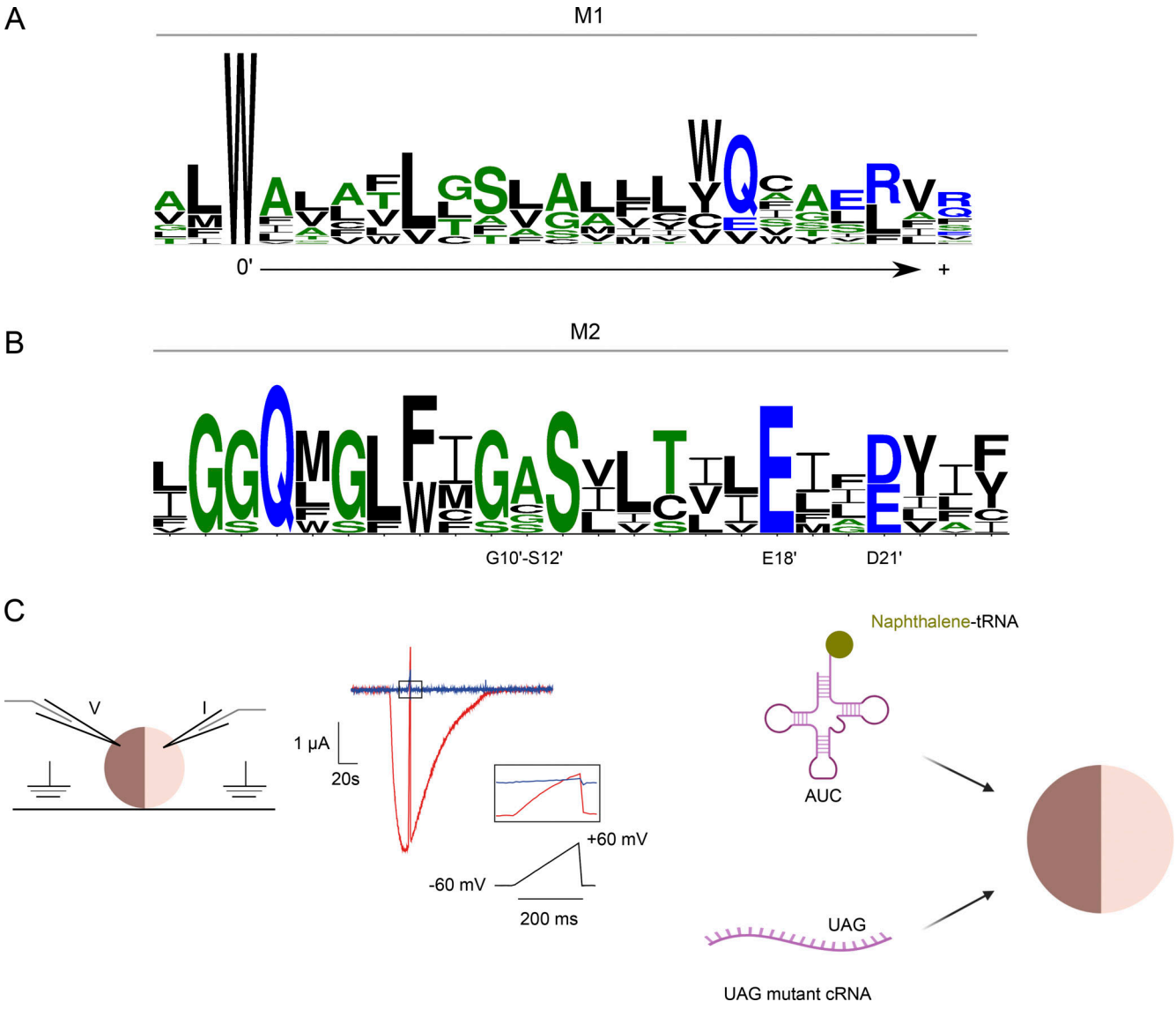

Figure S1. **M1 and M2 sequence logos and overview of nonsense suppression approach. (A)** Sequence logo of M1 and M2 based on mammalian ASIC an ENaC sequences (see Figs. S2 and S3). Residues are numbered according to position in mASIC1a. The height of each residue is proportional to its frequency at this position. Here, we have employed a numbering system for M1 in which equivalent residues from ENaCs and ASICs are referred to with the same number. The conserved W in M1 is designated the 0′ position. **(B)** Experimental approach used to determine ion selectivity of mASIC1a constructs. cRNA encoding WT or mutant mASIC1a was injected into *Xenopus* oocytes, and reversal potentials with extracellular Na^+, K^+, Li^+, and Cs^+ were determined using a 200-ms voltage ramp from −60 to +60 mV during the peak current. Currents during the voltage ramps at pH 7.4 (blue) were subtracted from currents during activating pH (red). **(C)** Incorporation of the ncAA naphthalene was achieved via the nonsense suppression method in *Xenopus* oocytes. The suppressor tRNA, THG73, lacking its terminal CA dinucleotide was enzymatically ligated to the ncAA naphthalene attached to a CA dinucleotide using an RNA ligase. The tRNA carrying naphthalene was injected into *Xenopus* oocytes together with mASIC1a mRNA containing an amber stop codon at the site of interest.

```
ASIC1a_HUMAN          ALWALCFLGSLAVLLCVCTERVQ
ASIC2a_HUMAN          VLWAVAFVGSLGLLLVESSERVS
ASIC3_HUMAN           GMWAAAVVLSVATFLYQVAERVR
ASIC4_HUMAN           TLWALALLTSLAAFLYQAAGLAR
ASIC5_HUMAN           VLWLVVVLGSVSLVTWQIYIRLL
ASIC1a_MOUSE          ALWALCFLGSLAVLLCVCTERVQ
ASIC2a_MOUSE          VLWAVAFVGSLGLLLVESSERVS
ASIC3_MOUSE           GLWATAVLLSLAAFLYQVAERVR
ASIC4_MOUSE           TLWALALLTSLAAFLYQAASLAR
ASIC5_MOUSE           VIWLAVVLGSVSLLVWQIYSRLV
ASIC1a_RAT            ALWALCFLGSLAVLLCVCTERVQ
ASIC2a_RAT            VLWAVAFVGSLGLLLVESSERVS
ASIC3_RAT             GLWATAVLLSLAAFLYQVAERVR
ASIC4_RAT             TLWVLALLTSLAAFLYQAASLAR
ASIC5_RAT             VIWLSVVLGSVSLLVWQIYSRLV
ENaCα_HUMAN           AFWAVLWLCTFGMMYWQFGLLFG
ENaCβ_HUMAN           AMWFLLTLLFAALVCWQWGIFIR
ENaCγ_HUMAN           LLWIGFTLTAVALILWQCALLVF
ENaCα_MOUSE           AFWAVLWLCTFGMMYWQFALLFE
ENaCβ_MOUSE           AMWFLLTLLFACLVCWQWGVFIQ
ENaCγ_MOUSE           LLWIAFTLTAVALIIWQCALLVF
ENaCα_RAT             AFWAVLWLCTFGMMYWQFALLFE
ENaCβ_RAT             AMWFLLTLLFACLVCWQWGVFIQ
ENaCγ_RAT             LLWIAFTLTAVALIIWQCALLVF
```

Figure S2. **Sequences used for the generation of the sequence logo of M1 segment.** Related to Fig. S1.

```
ASIC1a_HUMAN          IGGQMGLFIGASILTVLELFDYAY
ASIC2a_HUMAN          IGGQMGLFIGASILTILELFDYIY
ASIC3_HUMAN           IGGQMGLFIGASLLTILEILDYLC
ASIC4_HUMAN           LGGQMGLFIGASILTLLEILDYIY
ASIC5_HUMAN           LGGQLGLFCGASLITIIEIIEYLF
ASIC1a_MOUSE          IGGQMGLFIGASILTVLELFDYAY
ASIC2a_MOUSE          IGGQMGLFIGASILTILELFDYIY
ASIC3_MOUSE           IGGQMGLFIGASLLTILEILDYLC
ASIC4_MOUSE           LGGQMGLFIGASILTLLEILDYIY
ASIC5_MOUSE           VGGQLGLFCGASLITIIEIIEYFF
ASIC1a_RAT            IGGQMGLFIGASILTVLELFDYAY
ASIC2a_RAT            IGGQMGLFIGASLLTILELFDYIY
ASIC3_RAT             IGGQMGLFIGASLLTILEILDYLC
ASIC4_RAT             LGGQMGLFIGASILTLLEILDYIY
ASIC5_RAT             VGGQLGLFCGASLITIIEIIEYLF
ENaCα_HUMAN           LGSQWSLWFGSSVLSVVEMAELVF
ENaCβ_HUMAN           LGGQFGFWMGGSVLCLIEFGEIII
ENaCγ_HUMAN           FGGQLGLWMSCSVVCVIEIIEVFF
ENaCα_MOUSE           LGSQWSLWFGSSVLSVVEMAELIF
ENaCβ_MOUSE           LGGQFGFWMGGSVLCLIEFGEIII
ENaCγ_MOUSE           FGGQLGLWMSCSVVCVIEIIEVFF
ENaCα_RAT             LGSQWSLWFGSSVLSVVEMAELIF
ENaCβ_RAT             LGGQFGFWMGGSVLCLIEFGEIII
ENaCγ_RAT             FGGQLGLWMSCSVVCVIEIIEVFF
```

Figure S3. **Sequences used for the generation of the sequence logo of M2.** Related to Fig. S1.

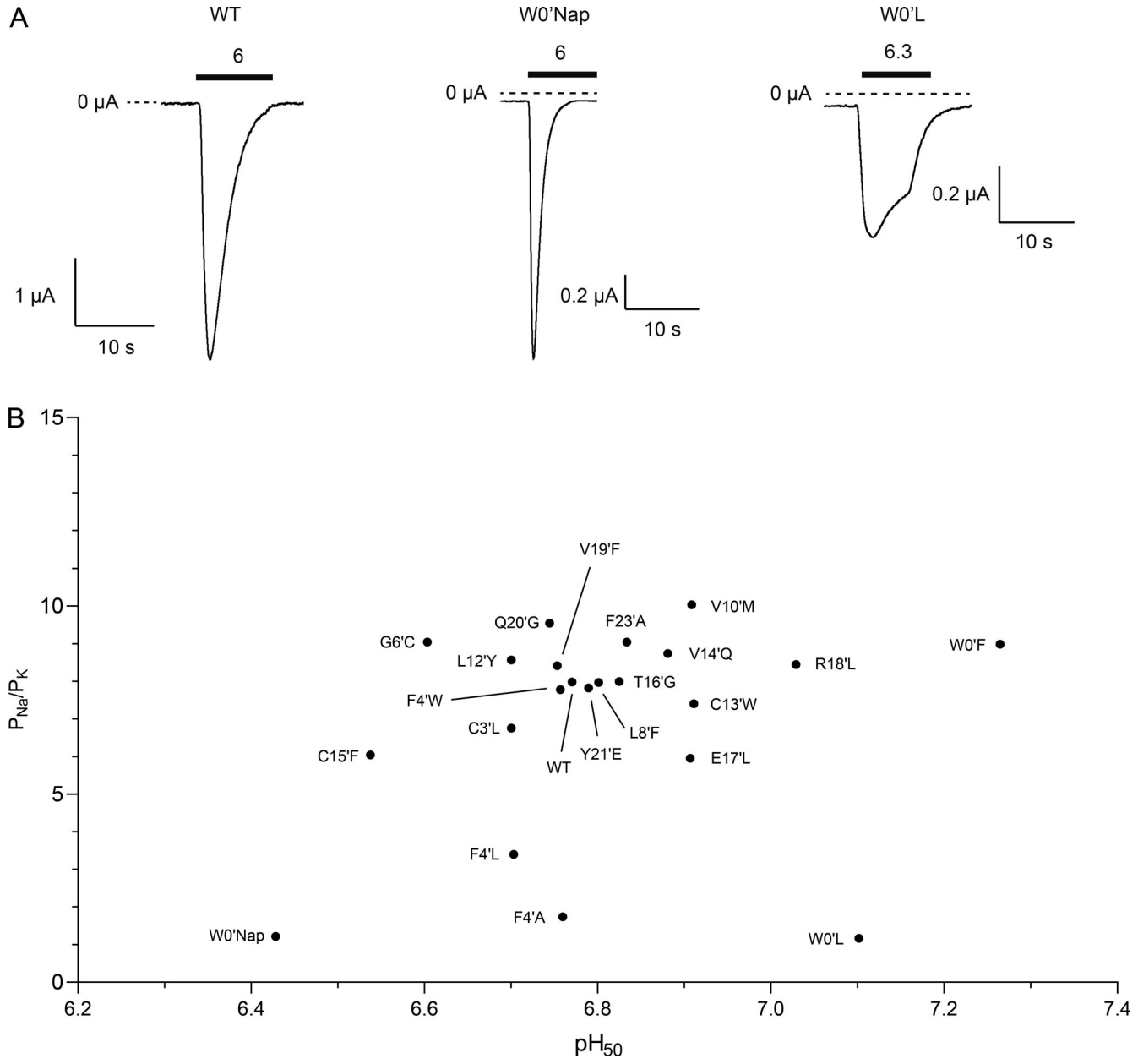

Figure S4. **Current traces of WT and designated mutant mASIC1a channels and effects of M1 mutations on ion selectivity and pH_{50}. (A)** mRNA encoding WT or mutant mASIC1a channels were injected into *Xenopus* oocytes, and currents were recorded using two-electrode voltage clamping. Cells were clamped at −20 mV and continuously perfused with ND96 solution (pH 7.4), and currents were elicited upon switching to ND96 solution with the designated pH. **(B)** Effects of M1 mutations on relative Na^+ over K^+ permeability ratios and pH_{50} are summarized with a scatterplot.

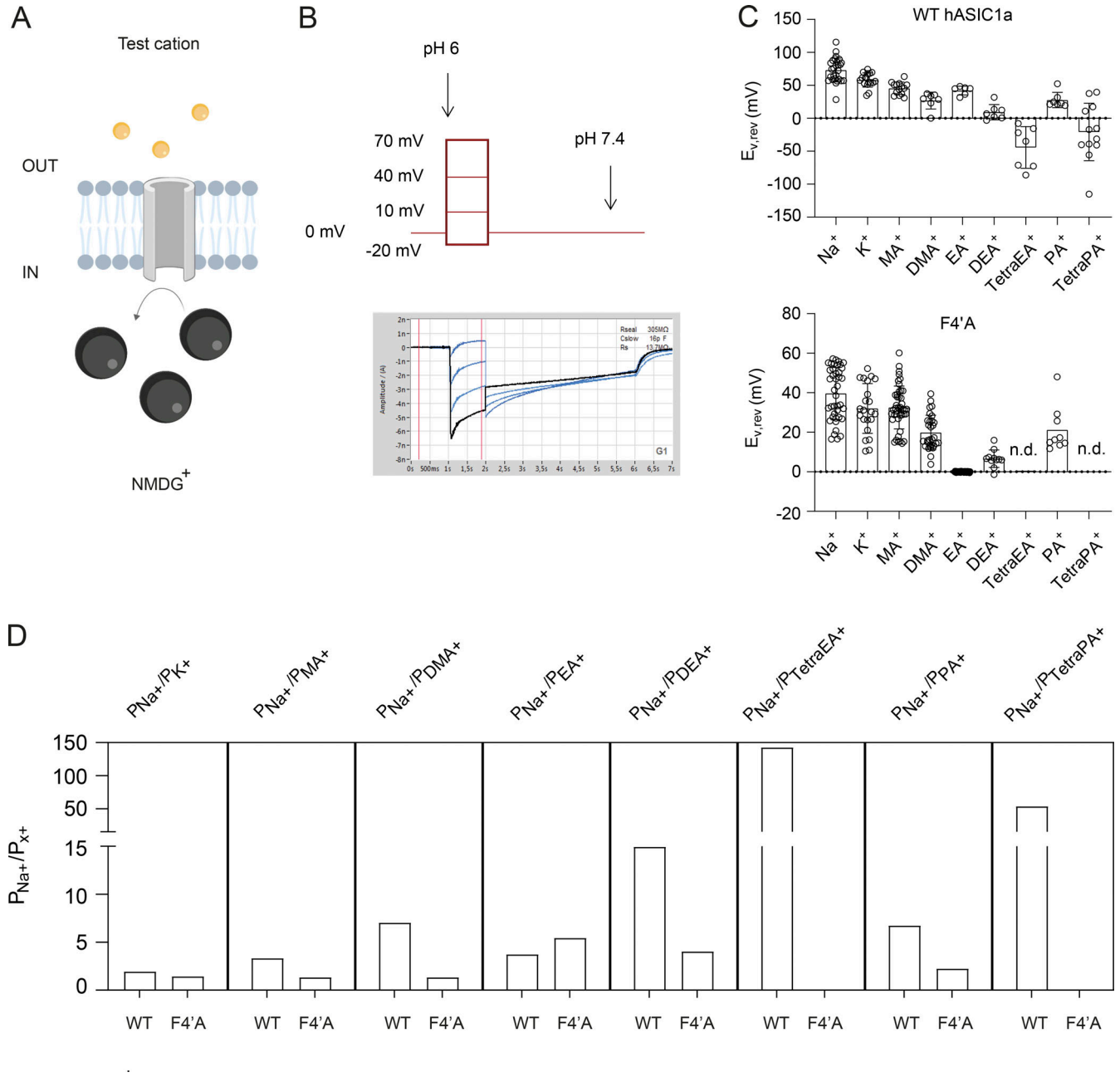

Figure S5. **Automated patch-clamp recordings using the SynchroPatch 384PE. (A)** Schematic illustration of the experimental setup. The ICS contained $NMDG^+$ as the only cation and was selected on the basis of its large size. The external side contained an ECS with one monovalent test cation. **(B)** The voltage protocol used to determine reversal potentials. ASIC1a knockout HEK293-T cells expressing either WT hASIC1a or the hASIC1a F50A mutant were clamped at 0 mV, and currents were recorded by stepping to the four voltages (−20, 10, 40, and 70 mV) in four sweeps upon the simultaneous application of a saturating concentration of protons (pH 6). A screenshot of an example current trace carried by extracellular Na^+ is shown in the inset below the protocol. **(C)** Reversal potentials estimated with different extracellular monovalent cations using the protocol shown in B. **(D)** Relative ion permeability ratios estimated for WT hASIC1a and the F4′A mutant, respectively.

```
Crassostrea_EKC42481.1   MLNNTSLHGVSKIS-----RGKTICHGVFWAVMTSVMLALLITVFVLYSLDYFLYETLI
Crassostrea_EKC39945.1   FADKTAMQGVGYIS-----SAKYWYSRAIWVFLLLVAMGWMVFHLYYLISQFTDLPVQT
Crassostrea_EKC42329.1   WLSAVDIHGLGIAG-----TTTHVLETSIWIIISCVAFSGFVFLVYLNFSVYYLQSSSF
XP_023240338.1           YEKRSNTKPPYIIA----WENSSKNKKK--LSRKKCSLSGFTYSSYKFLTNFFEYPVVV
Crassostrea_17580-23158  YGNSASFHGLRFVT----DPLANKPRRLIWLCLLTACLAVLVYQIVDRVTHFYSYPVTV
XP_023226921.1           FLGSSSVIGLSQIT-----KSRSIVRKLLWLAVLVTGLTFCAIESHKFMREFYKYPVVV
ENaCg_HUMAN              YCLNTNTHGCRRIV-----VSRGRLRRLLWIGFTLTAVALILWQCALLVFSFYTVSVSI
ENaCb_HUMAN              YCDNTNTHGPKRII----CEGPK--KKAMWFLLTLLFAALVCWQWGIFIRTYLSWEVSV
ENaCa_HUMAN              FCNNTTIHGAIRLV----CSQHNRMKTAFWAVLWLCTFGMMYWQFGLLFGEYFSYPVSL
ENaCd_HUMAN              FCTNATIHGAIRLV----CSRGNRLKTTSWGLLSLGALVALCWQLGLLFERHWHRPVLM
Crassostrea_EKC33938.1   FINETSFTAIARIV-----KANTILKKIIWLILVMAMMAWLTIQCYWLLDKYFSYPVEV
HyNaC2_157886734         YVQTSTLHGFRFIF-----MDTFIVRRVLWTILTLTMATIFFKELRNSINLFYEYPFTT
HyNaC5_289169249         YIEASTLHGYAYVC-----SDTFYIRRVLWAVLMLLGGIYFVFKLKVGIIEYFQYPFST
HyNaC6_594592304         YVESSTLHGFCYVC-----GDTFLVRRVLWALLMILGAIYFIIKLRYGIEEYLNYPFST
HyNaC7_594592306         YIESSTLHGFCYVC-----MDTFLGRRLIWAVLMILGAIYFIFKLRYGIKEYFDYPFST
ASIC2b_HUMAN             SLSRAKLHGLRHMCAGRTAAGGSFQRRALWVLAFCTSFGLLLSWSSNRLLYWLSFPSHT
bASIC_HUMAN              FAISTSFHGIHNIV-----QNRSKIRRVLWLVVVLGSVSLVTWQIYIRLLNYFTWPTTT
Crassostrea_EKC39946.1   NSRNSGLFGLGS---------------SPWEA----------------------------
ASIC1a_HUMAN             FASSSTLHGLAHIF----SYERLSLKRALWALCFLGSLAVLLCVCTERVQYYFHYHHVT
ASIC1b_HUMAN             FANSCTLHGTNHIF----VEGGPGPRQVLWAVAFVLALGAFLCQVGDRVAYYLSYPHVT
ASIC2a_HUMAN             FANTSTLHGIRHIF----VYGPLTIRRVLWAVAFVGSLGLLLVESSERVSYYFSYQHVT
ASIC3_HUMAN              FASNCSMHGLGHVF----GPGSLSLRRGMWAAAVVLSVATFLYQVAERVRYYREFHHQT
ASIC4_HUMAN              FASTSTLHGLGRAC----GPGPHGLRRTLWALALLTSLAAFLYQAAGLARGYLTRPHLV
Crassostrea_EKC22488.1   LGSESNAHGLAKIA-----MSRKTKRKVMWSLLVIIGFTAAAIHLSFLVIKYLQYNVVE
XP_023219716.1           IFKESSIPGVNNIA-----AAKGKFERFIWIFIVICCLTGFIYQVTLFLRHYYNYPTRV
XP_023215424.1           FAYRSSAHGIPRIA-----SSQNRFRRFMWIIVFLVAVAGFAYHSIYLILTYLSYPRMT
XP_023244170.1           FAYRSSAHGVQRIA-----SSQDNARRLMWSVVFLFAIAGCGFHSVYLILTYLSYPRMT
HyNaC8_594592308         MAVNSSFHGINYIC-----DSTYKVRRIIWIVVTLTAMLYAMREVYESTRKYLNYPVST
HyNac9_594592310         LIKNVSFHGLSYVA----DKRNNYFRRAIWFLITVGAFIYAVEKVYESTVNYFSYPFKT
HyNaC10_594592312        AGENISIHGLSHVF----DKRENFICRTVWLLITIAAFGYAVQKVYESTLNYFSYPFST
HyNaC4_157886739         MIDNSSFHGISYIA----GKENHFIRRTIWLLITMTAFGYAAQKVYESTVNYFSFPIST
HyNaC3_157886737         MIDNSSFHGLSYIF-----DKRHSIRRTIWFFITIAAFVYAMQKVYESTMNYFSYPFYT
HyNaC11_594592314        MIDNSSFHGLSYIF-----DKRHSVRRTIWFFITIAAFAYAMQKVYESTMNYFSYPFYT
```

Figure S6. **Sequences used for the generation of the sequence logo.** Related to Fig. 4.

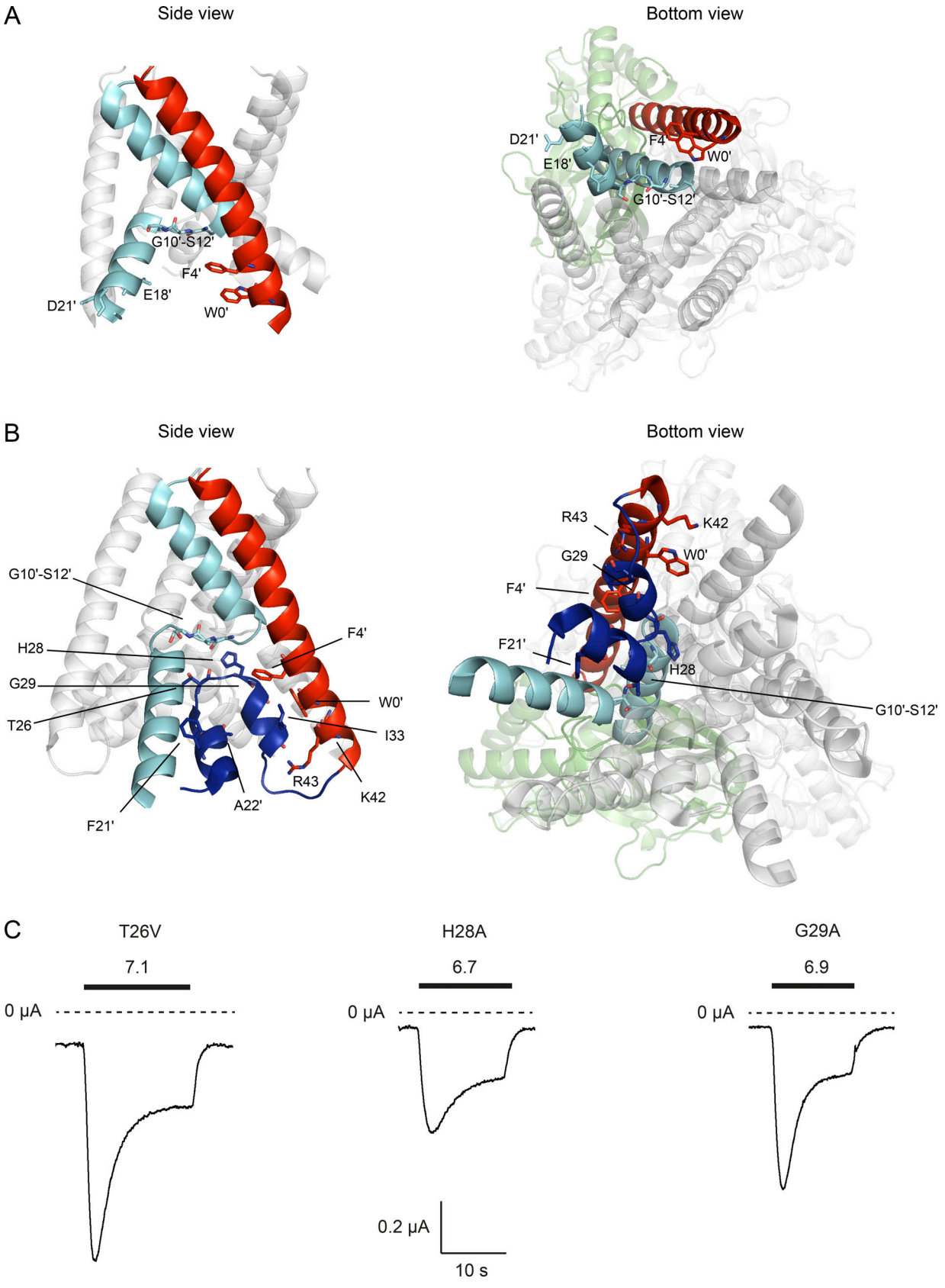

Figure S7. **cASIC1 structures and example current traces of selected pre-M1 mASIC1a mutants. (A and B)** Side view (left panel) and bottom view (right panel) of cASIC1 structures in an open (Protein Data Bank accession no. 4NTW; A) and desensitized state (Protein Data Bank accession no. 6VTK; B) with residues critical for ion selectivity shown as sticks. Blue, N; red, O. **(C)** Example traces of designated mASIC1a pre-M1 mutants recorded with two-electrode voltage clamping at −20 mV in *Xenopus* oocytes (applied pH defined above the black bar indicating length of ligand application).